Changes in anelasticity and grain boundary processes with stress cycling in semibrittle salt-rocks

J. Ding[1*], F. M. Chester[1], J. S. Chester[1], X. Shen[2#], and C. Arson[2]

[1]Center for Tectonophysics, Department of Geology & Geophysics, Texas A&M University, College Station, Texas.

[2]School of Civil and Environmental Engineering, Georgia Institute of Technology, Atlanta, Georgia.

Corresponding author: Jihui Ding (jihuid@stanford.edu)

*Current address: Department of Geophysics, Stanford University, Stanford, California.

#Current address: Department of Civil and Environmental Engineering, Northwestern University, Evanston, Illinois.

Key Points:

- Semibrittle salt-rock deformation involves coupled operation of grain boundary opening, grain boundary sliding, and dislocation glide
- The activation of frictional grain boundary sliding redistributes water facilitating diffusion processes
- Fluid-assisted diffusion leads to pronounced hysteresis and anelasticity controlled by the viscous sliding of closed grain boundaries

Abstract

The coupled operation of fracture, diffusion, and intracrystalline-plastic micromechanisms during semibrittle deformation of rock is directly relevant to understanding crustal processes such as earthquake rupture at the base of the seismogenic zone and failure of salt caverns for energy storage. Triaxial stress-cycling experiments are used to investigate elastic-plastic and viscoelastic behaviors in two synthetic salt-rocks deformed at room temperature and low confinement. During semibrittle flow at high differential stress, porous, granular, work-hardened samples deform predominantly by grain boundary sliding and opening accompanied by minor intragranular cracking and dislocation glide. In contrast, fully annealed, near-zero porosity samples deform at lower differential stress by dislocation glide, grain-boundary sliding and opening accompanied by minor intragranular cracking. During high-stress cycling and semibrittle flow, grain boundary sliding is predominantly frictional; but, associated dispersal of water previously trapped in fluid inclusions can activate fluid-assisted diffusional sliding along grain boundaries at low strain rates. Young's modulus and Poisson's ratio are largely controlled by the behavior of closed grain boundaries. Grain boundary sliding accommodated by fluid-assisted diffusion leads to nearly complete stress relaxation after semibrittle flow, and in subsequent low-stress cycling both viscoelasticity and pronounced hysteresis are observed. However, such time-dependent effects vanish with grain boundary healing over days-long holds at low differential stress. Experimental results suggest that within the semibrittle regime, high-stress events can lead to significant transient reduction in viscosity and related phenomena.

Plain Language Summary

Rock consists of small grains. The shape of bulk rock changes in response to loading. Scientists study processes occurring at scales of grain size or below that are responsible for the bulk shape changes. When multiple processes occur, their interaction and combined effects become quite complex. The coexistence of multiple processes is found in subsurface where earthquakes are generated and underground salt structures that are used for storing energy or nuclear wastes. Therefore, developing a good understanding of combined operation of multiple processes is necessary. In this study, synthetic salt-rocks are tested under cyclic loading at conditions that invoke multiple processes. Recoverable and permanent changes in bulk rock shape are measured. Features in salt grains are observed using a microscope. Experimental results show that opening and sliding of grain boundaries is mainly responsible for causing permanent shape change. Water at grain boundaries strongly affects how bulk rock shape change. With sufficient water and slow loading, the sliding of grain boundaries is assisted by water which causes the recoverable shape change to depend on loading rate. These findings indicate that processes occurring at grain boundaries may play an important role in controlling both recoverable and permanent changes in bulk rock shape.

1 Introduction

Rock deforms by a variety of microprocesses, including brittle processes of fracturing and frictional sliding as well as viscous processes of crystal-plasticity and diffusive mass transfer (Knipe, 1989; Sibson, 1977, 1986; Tullis, 1979). Semibrittle deformation refers to the mixed mode of brittle and viscous processes both of which contribute significantly to the total deformation (Carter & Kirby, 1978; Chester, 1989; Paterson & Wong, 2005; Reber & Pec, 2018). Much research has been directed to understand this rather complex deformation regime in different rock-forming materials at a wide range of pressure, temperature, and strain rate

conditions (Carter & Kirby, 1978; Chester, 1988, 1989; Hadizadeh & Tullis, 1992; Kirby & Kronenberg, 1984; Marti et al., 2017; Reber et al., 2015; Reber & Pec, 2018). Semibrittle deformation is directly relevant to many geologic processes in the crust, in particular earthquake generation. At the base of the seismogenic zone of the crust, abundant microstructural evidence has pointed to the mixed mode of frictional and viscous processes in felsic silicates (Fusseis & Handy, 2008; Mitra, 1984; Stewart et al., 2000; White & White, 1983; Zulauf, 2001). This transition zone connects the overlying fully brittle zone with the underlying fully viscous zone, which often corresponds to the depth limit of shallow crustal seismicity and experiences pronounced seismic stress cycling (Brace & Kohlstedt, 1980; Sibson, 1983). Semibrittle deformation is also highly relevant to engineered structures of salt formations. Salt caverns for energy storage typically operate at low pressure (a few to tens of megapascals) and low temperature (below 90°C) (Bérest, 2013; Ozarslan, 2012; Wang et al., 2018a). Under such conditions, brittle processes of fracturing and frictional sliding are expected to occur in addition to viscous processes of crystal plasticity and pressure solution (Chester, 1989; Hunsche & Hampel, 1999; Minkley et al., 2015; Munson et al., 1999; Peach & Spiers, 1996). The semibrittle deformation in salt caverns evolves spatiotemporally in response to cyclic stressing during cavern service cycles.

Although individual microprocess (e.g., dislocation creep, pressure solution) operating at near steady state conditions are relatively well understood, the interplay among them is inherently complex and requires further studies. Brittle and viscous processes may interact in a variety of ways and affect both elastic and inelastic deformation. For example, there are experimental evidences that intracrystalline plasticity affects microcracking process (Fredrich et al., 1989; Hirth & Tullis, 1994), and that grain boundary sliding may significantly lower elastic moduli of polycrystals (Ghahremani, 1980; Zener, 1941). The way through which these microprocesses are coupled dictates the rheologic behavior of the deformation transition zone (Bos & Spiers, 2002b; Chester, 1988; Pec et al., 2016; Shimamoto & Noda, 2014). More work is needed to elucidate how the combined operation of brittle and viscous microprocesses affects both elastic and inelastic deformation.

Semibrittle deformation are controlled by environmental conditions including pressure, temperature, and strain rate. While confining pressure and temperature are often stable in the subsurface, stress and strain rate may drastically change because of natural or anthropogenic processes. For example, major earthquakes impose periodic stressing during seismic ruptures, which may extend all the way to the base of seismogenic zone and possibly into the creep zone below (Ellis & Stöckhert, 2004; Ivins, 1996; Matysiak & Trepmann, 2012; Nüchter & Stöckhert, 2008; Scholz, 2019). Such pronounced stress and strain rate cycling would inevitably activate transient coupled microprocesses. Stress cycling is also common in salt caverns for energy storage (Bérest, 2013; Brouard et al., 2012; Lux & Dresen, 2012; Wang et al., 2018b). As energy medium (e.g., natural gas, crude oil) is filled and extracted from salt caverns during service cycles, changes of stress state around salt cavern walls would also induce transient semibrittle deformation.

Salt-rock has been studied not only for its direct relevance to salt tectonics and engineered salt structures, but also as analogues to other rock types. Comparing to silicate minerals, semibrittle and viscous microprocesses can be more easily activated at laboratory pressure, temperature, and strain rate conditions, which allows studying a broad range of steady state and transient micromechanisms (Bos & Spiers, 2002a; Carter & Hansen, 1983; Chester,

1988; Desbois et al., 2008; Niemeijer et al., 2008; Noda & Takahashi, 2016; Shimamoto, 1986; Shimamoto & Noda, 2014; Spiers et al., 1990; Urai et al., 1986). The rich research on salt-rock deformation has illuminated our understanding of similar microprocesses in other rock-forming minerals.

In this paper, we report an experimental investigation aimed at understanding how elastic properties (i.e., Young's modulus and Poisson's ratio) evolve with progressive inelastic deformation and underlying micromechanisms for both elastic and inelastic deformation in the semibrittle field. Two types of synthetic salt-rocks with contrasting microstructures (i.e., porosity, dislocation density, grain size and shape) are deformed using cyclic loading at room temperature and low confinement to activate semibrittle deformation. Inelastic deformation was investigated by cyclic loading through yield to determine mechanical behavior during progressive semibrittle flow. To investigate time-dependent elastic behavior (viscoelastic, anelastic), three strain rates (3×10^{-5}, 3×10^{-6}, and 3×10^{-7} s^{-1}) are applied in small-magnitude stress cycles where elastic parameters are determined. The stress relaxation technique is also employed to aid understanding of deformation mechanisms. Additionally, microstructures of key samples are characterized to provide necessary information relating elastic and inelastic deformation with micromechanisms.

2 Methods

2.1 Fabrication of two synthetic salt-rocks

Reagent-grade granular salt (99 wt.% NaCl) was used to fabricate two distinct synthetic salt-rock with contrasting microstructure: the "consolidated" and the "annealed" samples. The consolidated samples were fabricated through uniaxial consolidation of 0.3-0.355 mm diameter granular salt at a displacement rate of 0.34 mm/s, a temperature of 150 °C, and a maximum axial stress of 75 MPa. Procedures for uniaxial consolidation can be found in Ding et al. (2016). The annealed samples were produced by uniaxial consolidation followed by annealing. The consolidation step was the same as used for the consolidated samples, except that consolidation temperature and maximum axial stress were changed to 100 °C and 120 MPa, respectively. For annealing, the consolidated samples were sealed and placed in a pressure vessel at a temperature of 150 °C and a hydrostatic pressure of 100 MPa for a duration of 1 week. Fabricated samples are right-circular cylinders (19 mm diameter and 43 mm length), so from measurements of dimensions and mass, the starting bulk porosity of consolidated and annealed samples were 5.45 ±0.06% and 0.54±0.08%, respectively.

The rheological behavior of salt-rock can be greatly influenced by the amount of water in sample (Urai et al., 1986; Watanabe & Peach, 2002). Using a Fourier transform infrared (FTIR) spectrometer (method described in (Ding, 2019), water contents of consolidated and annealed samples were determined as 301.22±18.01 and 5.10±0.44 (weight $H_2O/10^6$ NaCl), respectively. To ensure consistency in water content after fabrication, samples were stored and handled in a controlled low-humidity glove-box where relative humidity was maintained below 17% (Ding et al., 2016).

Consolidation produced high dislocation density in halite grains by intracrystalline-plastic deformation, and subsequent annealing removed dislocations through recrystallization (Peach & Spiers, 1996). Overall, the consolidated samples are characterized as granular, porous aggregates of work-hardened grains with both intragranular and grain boundary inclusions of

water, whereas the annealed samples are a fully recrystallized and recovered, dense polycrystalline rock with less water overall and predominately in inclusions along grain boundaries (Ding, 2019). Qualitatively, the consolidated samples may be characterized as wet, whereas the annealed samples are dry (Watanabe & Peach, 2002).The consolidated samples are analogous to the pre-compacted and hardened salt aggregates that are often used to backfill salt repositories (Salzer et al., 2007), whereas the annealed samples are similar to natural salt-rocks free from recent deformation (Carter & Hansen, 1983). The contrasting microstructure and water content of the two synthetic salt-rocks allowed detailed study of microstructural control on the mechanical behavior of salt-rock.

2.2 Cyclic triaxial compression and stress relaxation experiments

The tests were performed at room temperature and a confining pressure of 1 MPa (**Table 1**) in a triaxial apparatus well suited for deformation experiments on weak geomaterials (Coble et al., 2014; French et al., 2015; Kitajima et al., 2012). While maintaining a constant confining pressure and using a constant axial displacement rate, the differential stress in the direction of sample axis was varied in two types of load cycles: 1) small-load cycles in which differential stress was cycled between 0 and ~6.5 MPa and the sample deformed elastically, and 2) large-load cycle in which differential stress was cycled between zero and the flow strength, and the sample was deformed permanently by a specified increment of axial shortening before the unload portion of the cycle (**Figure 1**). Except for those performed at zero axial strain, small-load cycles were started ~15 minutes after the preceding unload from flow strength was completed to ensure a consistent amount of rest time before initiating measurements of anelasticity in all tests. This step reduced the impact of time-dependent deformation from large-load cycles on subsequent small-load cycles. A constant strain rate of 3×10^{-6} s^{-1} was used for large-load cycles, while three different strain rates of 3×10^{-5}, 3×10^{-6}, and 3×10^{-7} s^{-1} were used in small-load cycles to investigate the rate-dependence of anelastic behavior. Axial and radial strains were measured by two rosette strain gauges of 0.25-inch gauge length and 350 Ω resistance. Strain gauges were glued at opposing sides of the sample and averaged to account for sample tilting during deformation tests (**2**), although the differences in strain measurements of a sample is less than 0.6%. Differential force was measured through a semi-internal force gauge that is in direct contact with sample assembly and unaffected by the friction between the loading piston and sealing stack. The differential force gauge and confining pressure are accurate to ±70 N, ±0.01 MPa, respectively. The triaxial deformation apparatus used in this study has been described in greater detail by French et al. (2015).

193
194 Table 1. Sample classification and experiments[a] performed

Sample No.	Sample type	Final axial strain (%)	Test performed	Notes
60209R	Granular	N/A	N/A	sectioned
70516	Consolidated	N/A	undeformed	sectioned
61003	Consolidated	2.77[b]	cyclic loading	sectioned
61123	Consolidated	7.31[b]	cyclic loading	sectioned
80204	Consolidated	8.79	stress relaxation	sectioned
80306	Consolidated	3.82	cyclic loading, hold	first-round of cyclic loading
80306	Consolidated	3.79	cyclic loading	second-round of cyclic loading
61030	Annealed	N/A	undeformed	sectioned
70304	Annealed	4.87[b]	cyclic loading	sectioned
70305-2	Annealed	3.51	cyclic loading, hold	first-round of cyclic loading
70305-2	Annealed	2.96	cyclic loading, hold, stress relaxation	second-round of cyclic loading

195 [a]All experiments were conducted at room temperature and a confining pressure of 1MPa.
196 [b]Final axial strains equivalent to strain gauge measurements were estimated based on total axial strains measured by
197 an external DCDT and experiments with both strain gauge and DCDT strain measurements (i.e., sample 80306 and
198 70305-2)

199

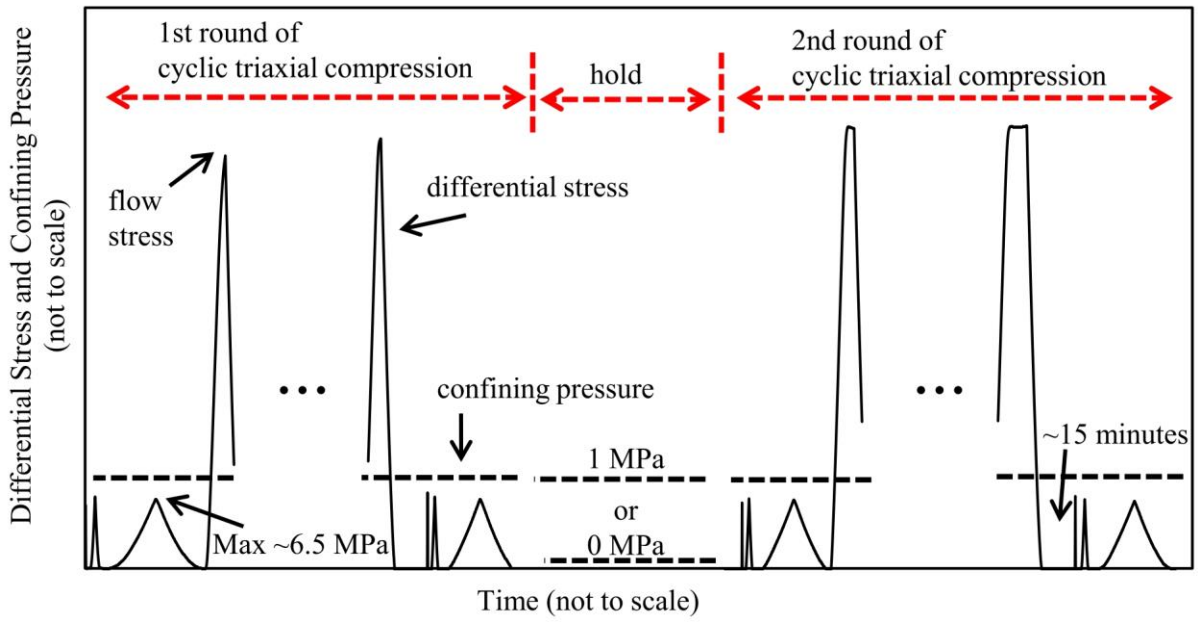

200
201 Figure 1. Schematic of load paths of cyclic triaxial compression test. Small- and large-load stress cycles
202 and hold between cyclic loading tests are illustrated.

203

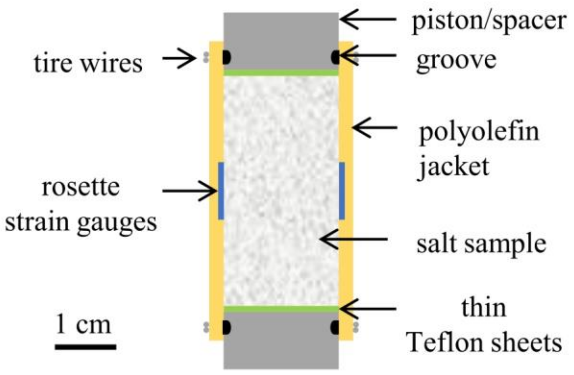

Figure 2. Schematic of sample assembly.

To investigate the time dependence of changes in elastic properties, a "hold" was employed between two rounds of cyclic loading tests on the same sample. The salt-rock sample was first deformed to approximately 4% axial strain, close to the linear limit of the strain gauges (4.5%), to record the evolution of elastic properties with axial strain. Then the sample was removed from the vessel and the strain gauges were replaced, after which samples were held at either at 0 or 1 MPa confining pressure for a period of time (1-5 days). After the hold, a second-round of cyclic loading was performed on the sample following similar stress cycles as used in the first-round (**Figure 1**).

Stress relaxation tests also were conducted to gain more information on time-dependence and deformation mechanisms (**Table 1**). The loading piston was abruptly stopped when a sample was being deformed at a constant strain rate. Differential stress on the sample decreases with time as elastic energy stored in the sample and loading rig is converted into inelastic strain. The stress relaxation technique allows determination of inelastic deformation mechanisms through the analysis of strain rate versus stress behavior (French et al., 2015; Rutter et al., 1978).

2.3 Microstructural characterization

Loosely packed salt grains, the consolidated and annealed synthetic salt-rock samples, and key synthetic salt-rock samples deformed in triaxial compression, were epoxy-saturated, cut along the cylinder axis, and polished to make petrographic sections, and then chemically etched to allow observation of grain-scale features, including grain boundaries and dislocations (**Table 1**). All steps of cutting and polishing samples were carried out using the low-humidity glove-box. The sectioning and etching procedures follow the techniques developed by Spiers et al. (1986) with minor modifications. Microstructures were characterized under both reflected- and transmitted-light. Observations focus on the central part of the sample, where the strain gauges were attached, for the benefit of direct correlation between microstructures and mechanical data as well as reduced sample end-effects. In addition to detailed observation on a few halite grains in a single photomicrograph of an area 1 mm^2 or smaller, tens of images were stitched together to allow observation of one to two hundred grains in an area of approximately 20 mm^2, which is equal to about 40% of the strain gauge area.

3 Results

3.1 Mechanical behavior

3.1.1 Overall stress-strain behavior

At room temperature and a confining pressure of 1 MPa, the mechanical behavior of the consolidated samples is characterized by approximately linear elastic deformation, yielding at approximately 36 MPa, followed by inelastic deformation at relatively constant stress of ~40 MPa (**Figure 3a**). The inelastic deformation is homogeneous across the samples with only a slight barreling in the middle. In the beginning of the deformation experiment the sample compacts slightly and then steadily dilates thereafter, documenting a porosity increase. The semibrittle flow strength and rate of porosity increase for the two rounds of cyclic loading tests, separated by a 34.5 hour hold without confinement, are highly consistent (**Figure 3a**). At the same testing conditions used for the consolidated samples, the annealed samples show similar mechanical behavior except for yielding at lower stress (~13 MPa) and work-hardening at a progressively decreasing rate throughout the deformation test (**Figure 3b**). The final strength of the annealed samples is about 80% of the semibrittle flow strength of the consolidated samples. Dilatancy occurs at an increasing rate throughout the deformation test indicative of porosity development. Subsequent to the end of the first-round of cyclic loading, after the final unload and removal of confining pressure, annealed samples display apparent axial elongation as can occur by unloading cracks during depressurization. Visual inspection did not confirm any cracks, but microstructural observations document the presence of unloading cracks. After the sample undergoes an unconfined hold for 66 hours, the second-round cyclic loading was initiated. The first loading cycle shows apparent reduction in slope (Young's modulus) relative to earlier load cycles, likely from the presence of the unloading cracks. After imposing ~0.5% inelastic axial strain during the first load cycle, the subsequent unload-load cycles show greater slopes comparable with those of the first-round of cyclic loading test, indicating the unloading cracks produced during the unconfined hold are effectively closed during the first large-load cycle of the second round.

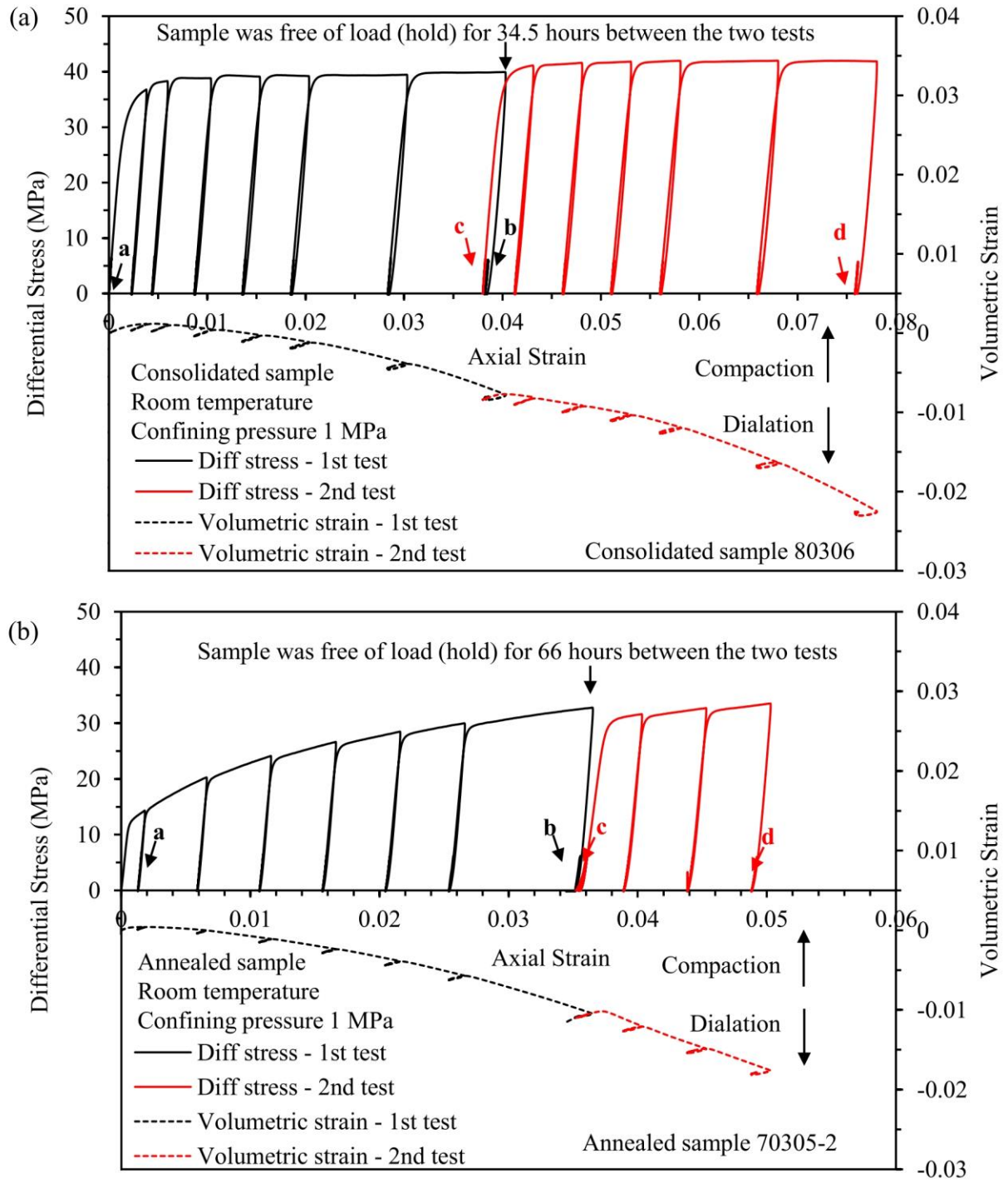

Figure 3. Plots of differential stress and volumetric strain versus axial strain for (a) consolidated sample 80306 and (b) annealed sample 70305-2. The first and last small-load cycles for each round of cyclic compression test are indicated by letters. Note small-load cycles are not readily seen due to scale and masking by large-load cycles.

3.1.2 Stress-strain behavior during small-load cycles

Small-load cycles of consolidated samples exhibit characteristic stress-strain behavior (**Figure 4**). For the first-round of cyclic loading at zero axial strain, before the first large-cycle loading, samples show nearly perfect-linear elastic deformation, and the subsequent small-load cycles of different strain rates overlie exactly (**Figure 4a**). As permanent axial strain increases with the large-load cycling, the elastic response during the small-load cycles progressively develops a non-linear elastic response with hysteresis that is rate-dependent. Slower loading and unloading lead to more compliant behavior and hysteresis (**Figure 4b**); however, even with hysteresis, the axial strain is nearly fully recovered during a single small load-unload cycle regardless of strain rate, whereas radial strain recovers more than initially achieved. During the ~15 minutes between complete unload of large cycles and start of small cycles, appreciable axial and radial strain is recovered providing evidence of anelasticity consistent with the rate-dependence of elastic behavior seen in the small-load cycles (**Figure 4b, d**). For the second-round cyclic loading test, after the days-long hold with no confinement, the behavior during the first small-load cycle (which precedes the first large cycle) shows that the sample recovers to the initial state (i.e., the state prior to initiating the first-round of small load cycling) where hysteresis and rate-dependence are absent (**Figure 4c**). With continued deformation, the sample displays the same evolution as in the first-round of cyclic loading before the hold, i.e., increasing rate-dependence and hysteresis with permanent strain (**Figure 4d**).

The small-load cycles of annealed samples show quite different stress-strain behavior from those of consolidated samples (**Figure 5**). Rate-dependence and hysteresis are absent throughout the deformation tests. Closing of unloading cracks is evident in the first small-load cycles of the second-round test (**Figure 5c**). Following small-load cycles show similar stress-strain behaviors as those of the first-round test (**Figure 5d**). Very little axial and radial strain is recovered during the ~15 minutes between complete unload of large cycles and the start of small cycles (**Figure 5b, d**).

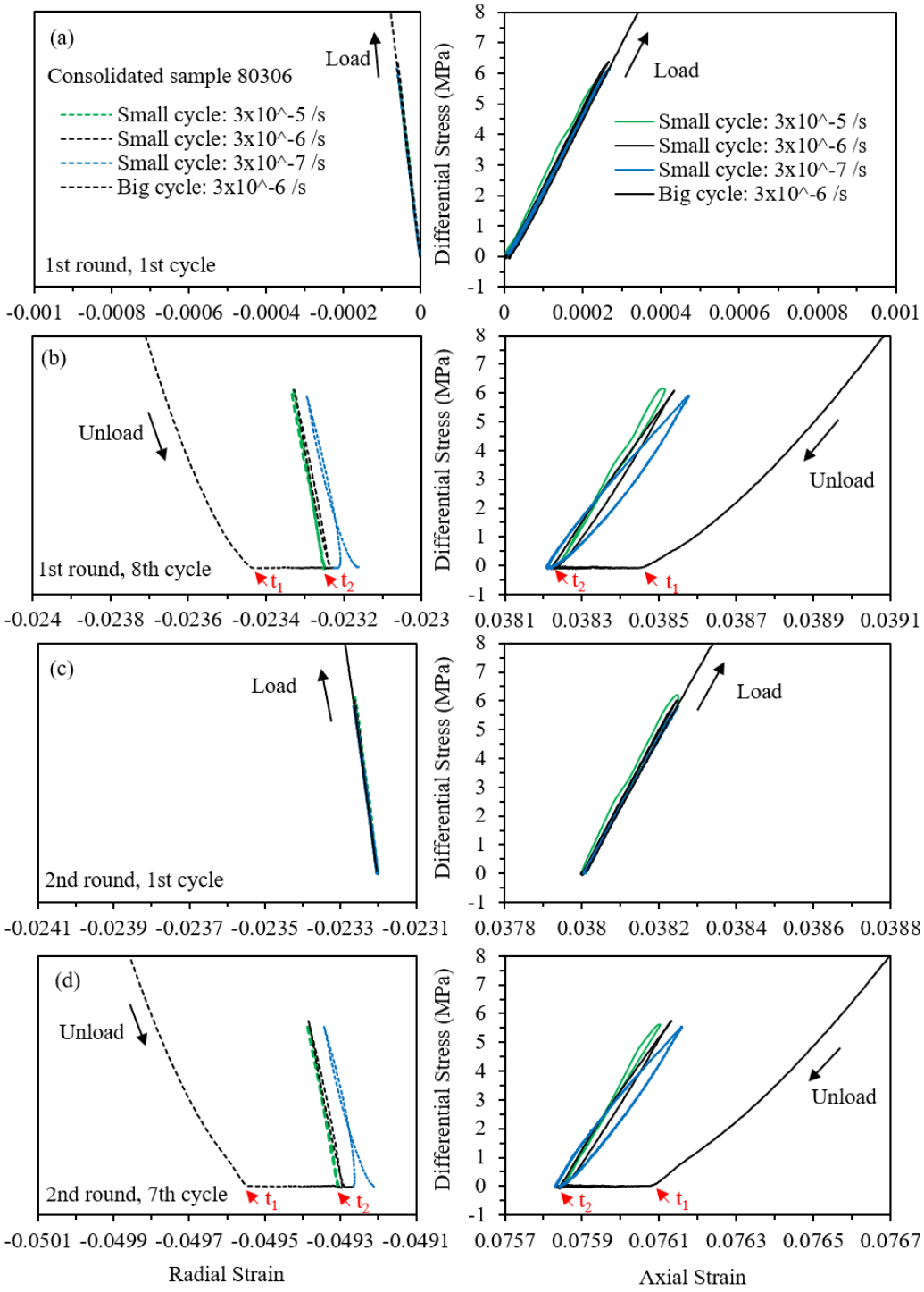

Figure 4. Plots of differential stress versus axial and radial strain of small-load cycles for consolidated sample 80306. The first and last small-load cycles for two rounds of cyclic compression tests are shown. Refer Figure 3 (a) for locations of these small-load cycles in the overall stress-strain curve. Loading and unloading directions of large-load cycles are indicated by arrows. t_1 and t_2 mark the complete unload of a large cycle and the start of the first small cycle, respectively. Approximately 15 minutes was maintained between t_1 and t_2 to reduce the impact of time-dependent deformation from large-load cycles on subsequent small-load cycles.

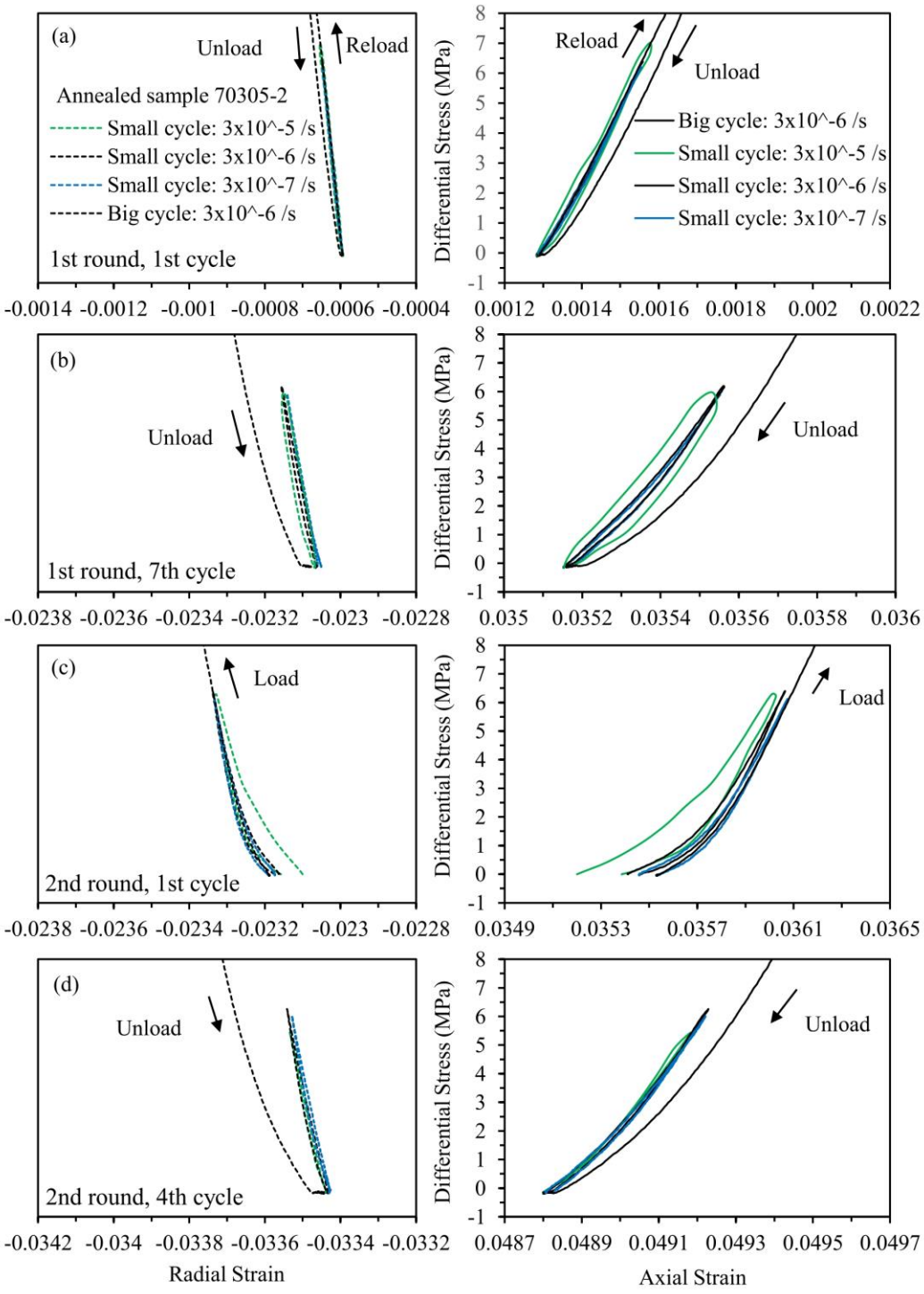

Figure 5. Plots of differential stress versus axial and radial strain of small-load cycles for annealed sample 70305-2. The first and last small-load cycles for two rounds of cyclic compression tests are shown. Refer Figure 3 (b) for locations of these small-load cycles in the overall stress-strain curve. Loading and unloading directions of large-load cycles are indicated by arrows. Note in (b) the amplified hysteresis of the fastest small-cycle (shown in green) was caused by the loading procedure, likely a sticking of force gauge during rapid loading/unloading.

3.1.3 Young's modulus and Poisson's ratio

Young's modulus and Poisson's ratio are determined for the differential stress range of 2.5 and 5.5 MPa using linear fitting to the stress-strain data of both the loading and unloading sections of the small-load cycles. This differential stress range covers a major part of the stress cycling of small-load cycles (between 0 and 6.5 MPa) and therefore reflects the overall slope of load cycles. As shown in the previous section, axial strain is nearly fully recovered during small-load cycles even when there is appreciable hysteresis. Therefore, the stress-strain behavior of small-load cycles is considered elastic. Young's modulus and Poisson's ratio are determined for stress intervals in loading and unloading for small (2.5-5.5 MPa) and large (18-21 MPa) cycles, which all show similar evolution in the magnitude of modulus with the permanent strain. Accordingly, only the Young's modulus and Poisson's ratios determined from the loading sections of the small-load cycles are presented (**Figure 6**).

For consolidated samples, Young's modulus of small-load cycles shows clear evolution with inelastic deformation (**Figure 6a**). Overall, for the first-round of cyclic loading, Young's modulus decreases with increasing inelastic deformation. At zero axial strain, Young's modulus at different loading rates are similar, but as inelastic deformation increases, they progressively diverge in magnitude. After the days-long hold, in the first set of small-load cycles of the second-round tests, the Young's modulus is nearly the same as the original values at zero axial strain and are similarly rate-insensitive. With further permanent strain in the second-round tests, Young's modulus decreases quickly and develops pronounced rate-dependence, repeating the evolution shown in the first-round test. Overall, Poisson's ratio increases with increasing inelastic deformation (**Figure 6b**). Similar to the evolution of Young's modulus, Poisson's ratio is initially rate-independent but progressively increases in rate-dependence with increasing inelastic deformation. After the hold, Poisson's ratio recovers significantly and returns to rate-independence, but then repeats the same evolution as seen in the pre-hold, first round tests.

Young's modulus of annealed samples exhibits a different evolution with increasing inelastic deformation than that of consolidated samples (**Figure 6c**). In the first-round test of an annealed sample, Young's modulus is similar in the first two small-load cycles, but then decrease continuously thereafter. In the second-round test, after a hold for 66 hours without confinement, the first small load cycles show abnormally low Young's modulus due to closing of the unloading cracks (**Figure 5c**). In subsequent cycles, Young's modulus maintains similar values slightly lower than those of the last cycles of the first-round test, without any sign of recovery to the original values (i.e., at zero axial strain). Unlike the consolidated sample, Young's modulus of annealed samples is rate-independent regardless of the imposed inelastic strain. Poisson's ratio of annealed samples increases with increasing inelastic strain (**Figure 6d**). Neither strain rate nor a long hold affects the evolution of Poisson's ratio.

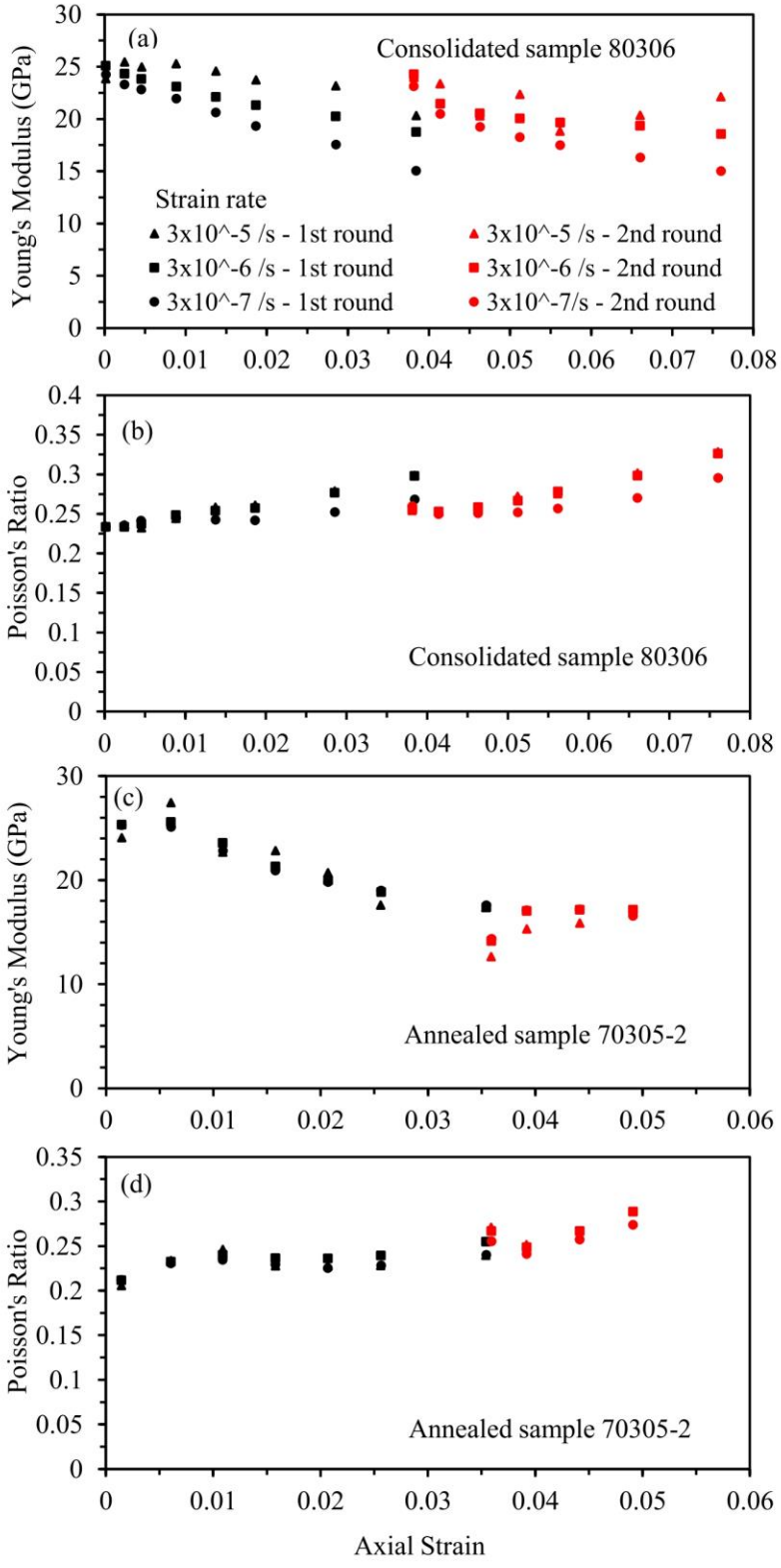

Figure 6. Plots of Young's modulus and Poisson's ratio as a function of axial strain for consolidated sample 80306 (a, b) and annealed sample 70305-2 (c, d). Young's modulus and Poisson's ratio were calculated for the loading segments of small-load stress cycles in the differential stress range between 2.5 and 5.5 MPa.

353 3.1.4 The effects of holds on elastic properties

354 As shown by the measurements of Young's modulus and Poisson's ratio, imposing a hold
355 leads to a recovery from the reduced values produced during permanent flow to nearly-original
356 values (prior to the permanent deformation). The recovery occurs very rapidly in consolidated
357 samples; experiments show the Young's modulus recovers to 96% of the original values in less
358 than 22 hours. The rapid recovery did not require confining pressure or differential stress.

359 Elastic properties of annealed samples do not recover after a hold at zero pressure for 66
360 hours, but only because of the presence of the unloading cracks (**Figure 5c**); recovery of elastic
361 properties does occur once unloading cracks are closed at 1 MPa confining pressure (**Figure 7**).
362 Nonetheless, compared to consolidated samples, recovery in annealed samples is much slower
363 even if the sample is under pressure and stress. After ~27 hours under confining pressure,
364 Young's modulus recovers to only 66% to 71% of the original value. With additional ~90 hours
365 under both pressure and differential stress (during stress relaxation test), Young's modulus
366 recovers to 89% of the original value.

367

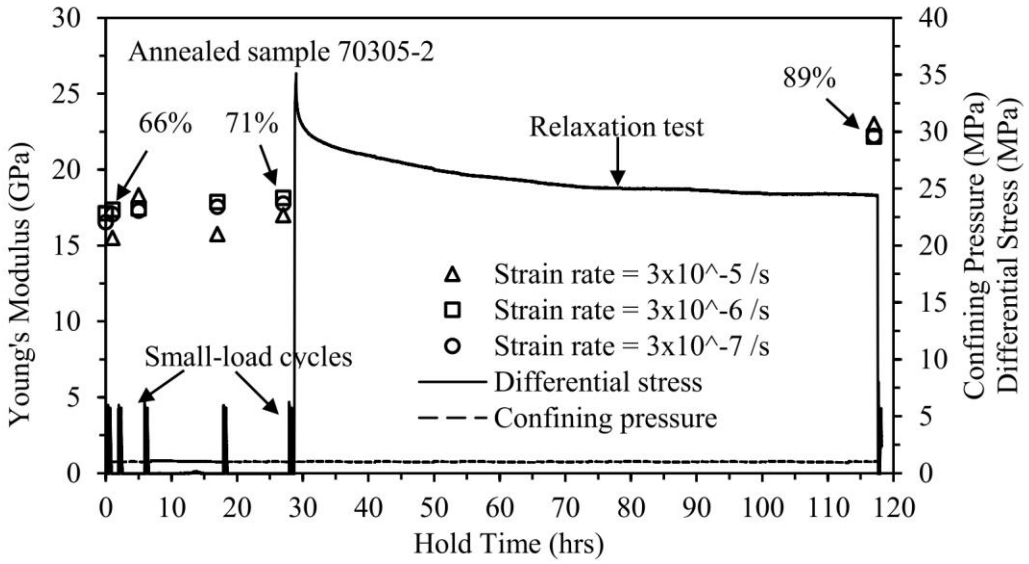

368

369 Figure 7. Plots of Young's modulus and differential stress as a function of hold time for annealed sample
370 70305-2. The hold time is relative to the end of the last (4th) small-load cycles of the second-round test in
371 Figure 3 (b). Percentage numbers are relative to the original Young's modulus (i.e., at zero axial strain).

372

373 3.1.5 Stress relaxation behavior

374 The stress relaxation tests were initiated at high differential stress after accumulating
375 permanent strain by semibrittle flow during a large load cycle. The stress relaxation was
376 continued until strain rate decreased to 1×10^{-9} s^{-1} or below. Qualitatively, the stress relaxation
377 behavior of the consolidated and annealed samples is markedly different. The consolidated
378 sample displays much greater relaxation of stress over a longer period of time before reaching a
379 strain rate of 10^{-9} s^{-1}, whereas the annealed sample displays less relaxation of stress over a
380 shorter period of time until strain rate reaches 10^{-9} s^{-1} (**Figure 8**).

Stress relaxation data of strain rate versus stress plotted in logarithmic scale may be used to identify operation of different time-dependent microprocesses by comparing the slope of the relaxation curve between the different samples and within a single sample as a function of stress. The slope corresponds to the stress exponents of rheologic flow laws and have characteristic values for micromechanisms such as dislocation glide and diffusion (Haupt, 1991; Spiers et al., 1986; Zhang et al., 2007). The slope of the stress relaxation curve for the consolidated samples reveals two distinct deformation regimes, one with a large stress exponent (8.8) at high strain rates and the other with a low stress exponent (0.9) at low strain rates (**Figure 8**). The transition between these two regimes is gradual, characterized by an inflection point at a strain rate of ~2 × 10^{-8} s^{-1}. The stress relaxation behavior of annealed samples shows only one regime having a high stress exponent (25) over the range of strain rate of 5×10^{-6} s^{-1} to as low as 4×10^{-10} s^{-1} (**Figure 8**).

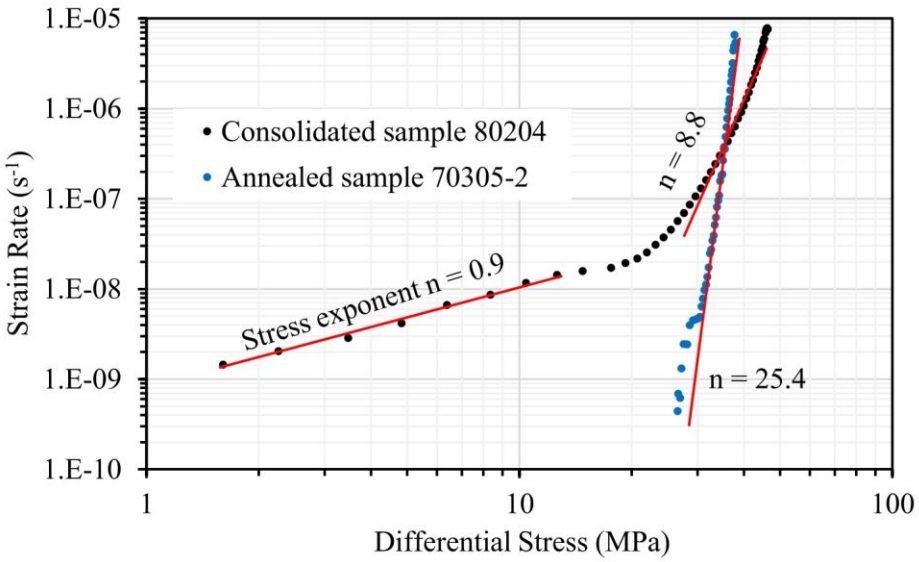

Figure 8. Plots of strain rate versus differential stress derived from stress relaxation tests for consolidated sample 80204 and annealed sample 70305-2. Stress exponents are determined for deformation regimes by linear fitting to data shown by the red lines.

3.2 Microstructures

3.2.1 Starting material

An unconsolidated sample of the as-received reagent-grade granular salt was epoxied, cut, polished and etched to observe the starting microstructure. The granular salt consists of cubic-shaped grains with fairly sharp corners, and show very little evidence of dislocation structures after etching (**Figure 9a**). Individual grains often contain fluid inclusions that appear as dark pits in the petrographic image. Fluid inclusions exhibit cubic, tubular or irregular shapes, and may be isolated or arranged in linear arrays. Fluid inclusion size varies from tens of microns to less than one micron.

After consolidation, the initially cubic grains have more rounded corners due to intracrystalline plastic deformation (**Figure 9b**). Grain contacts appear fully closed and are often

straight or only slightly curved. Pores (equant voids) are present at places where three or more grains come together. The dominant grain substructures are the well-developed, dense, linear etch features, termed slip lines. The wavy slip lines are indications of dislocation glide controlled by cross slip of screw dislocations (Senseny et al., 1992; Spiers & Carter, 1996). The slip lines within individual grains are generally similar in orientation reflecting crystallographic control. At grain contacts where deformation is most intense, sets of slip lines in two or more orientations intersect. In some of the most highly strained areas, high dislocation density led to development of recrystallized grains. The recrystallized grains, characterized by straight boundaries and dislocation-feature-free interiors, are usually small and uncommon (less than 4.8% of total grains). These recrystallized grains formed at the expense of the highly deformed grains, and likely at the latest stages of consolidation or after consolidation was terminated and under static conditions because the grain boundaries are straight and the interiors are largely devoid of slip lines. Minor intragranular cracks often intersect fluid inclusions or develop along fluid inclusion arrays, likely reflecting stress concentration at inclusions to nucleate cracks. Less than 6.4% of all grains show intragranular cracks, which indicates limited influence of brittle deformation during consolidation. Grain boundaries are well bonded with presence of dense and irregular-shaped fluid inclusions (**Figure 10a, b**). These grain boundary fluid inclusions typically measure less than 10 μm in length.

For the annealed samples, which are produced by annealing and static recrystallization of consolidated samples similar to that described above, comprised of strain-free, crudely polygonal grains forming imperfect triple junctions with some gently curved grain boundaries (**Figure 9f**). All grain contacts are fully closed and pores (e.g., voids at triple junctions) are not observed at the optical microscopic scale. Compared to the consolidated samples, annealing produced a smaller average grain size (0.241 mm) but with a much greater range of sizes (0.025-0.833 mm). No microcracks are observed in annealed samples. Grain boundaries are well bonded and display dense and nearly equal-dimension fluid inclusions that measure less than a few microns in diameter (**Figure 10e, f**). Annealing reduced the fluid inclusion density and removed most of the larger fluid inclusions in grain interiors consistent with the much lower water content than in consolidated samples.

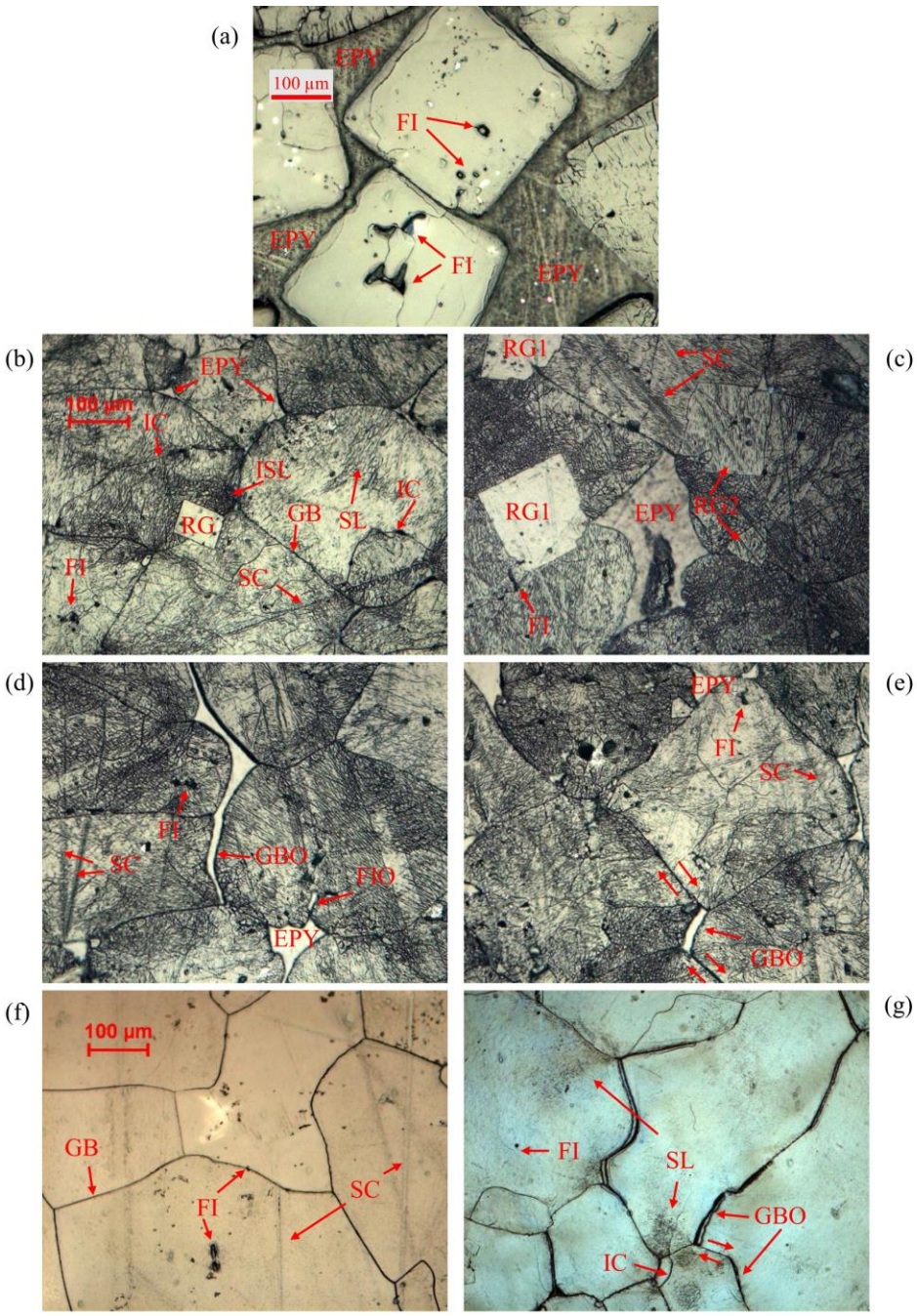

Figure 9. Reflected-light micrographs of (a) reagent-grade granular salt sample 60209R, (b) undeformed consolidated sample 70516, (c) consolidated sample 61003 deformed to 2.77% axial strain, (d) and (e) consolidated sample 61123 deformed to 7.31% axial strain, (f) undeformed annealed sample 61030, and (g) annealed sample 070304 deformed to 4.87% axial strain. Polished surface was chemically etched. GB – grain boundary, GBO – grain boundary opening, EPY – epoxy (pore), RG – recrystallized grain, SL – slip lines, ISL – intersected slip lines, FI – fluid inclusions intersected the polished surface, FIO – fluid inclusions opening, IC – intragranular cracks, SC – scratch resulted from polishing. Paired arrows show inferred shear motion. In deformed samples, differential load axis was vertical. Scale for (b), (c), (d) and (e) is shown in (b); scale for (f) and (g) is shown in (f). Note two types of recrystallized euhedral grains are shown in (c): RG1 – recrystallized grains free of dislocation, RG2 – recrystallized grains containing slip lines.

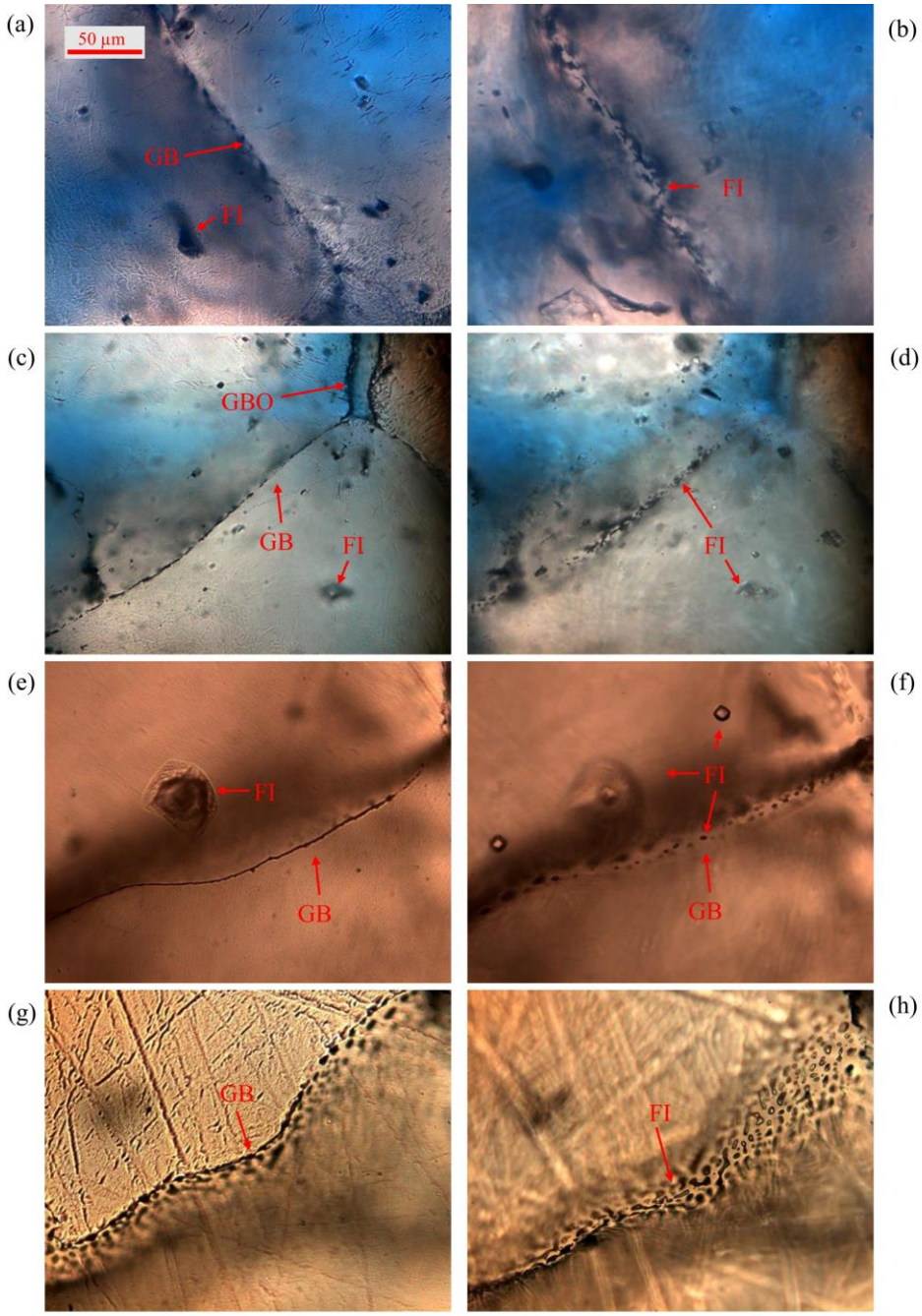

Figure 10. Transmitted-light micrographs of (a) and (b) undeformed consolidated sample 70516, (c) and (d) consolidated sample 61123 deformed to 7.31% axial strain, (e) and (f) undeformed annealed sample 61030, (g) and (h) annealed sample 70304 deformed to 4.87% axial strain. Optical focus for (a), (c), (e), and (g) is on the polished surface; optical focus for (b), (d), (f), and (h) is below the polished surfaces to reveal grain boundary structures. Polished surface was chemically etched. GB – grain boundary, GBO – grain boundary opening, FI – fluid inclusions intersected the polished surface. Differential load axis was vertical. Scale is shown in (a). Note fluid inclusions are observed inside all grain boundaries.

3.2.2 Deformed samples

Triaxial compression of consolidated samples led to an increase in the density of slip lines, characterized by an overall darker appearance in photomicrographs (compare **Figure 9b** with **c**, **d**, and **e**). Two sets of recrystallized grains are observed, but the fractional area of recrystallized grains is low, ranging from 3% to 7%. One set of recrystallized grains appear undeformed and show no sign of dislocation substructure, whereas the other set are slightly deformed and display wavy slip lines with similar characteristics to grains in consolidated samples (**Figure 9c**). The majority of recrystallized grains appear in euhedral shapes and reside either at grain boundaries or within highly deformed grains close to fluid inclusions. Grain shape analysis was performed on consolidated-samples triaxially-deformed to different axial strain to evaluate the role of grain flattening by intracrystalline plasticity. Grains were best-fit by ellipses with the same area as the grain to determine the minor to major axis ratios. Consolidated samples triaxially deformed to 0%, 2.77%, and 7.31% axial strain are characterized by grain axial ratios of 0.671±0.172 (131 grains), 0.650±0.174 (215 grains), and 0.639±0.162 (211 grains), respectively. The axial strain by grain flattening is estimated to account for around 6% of the total axial strain.

The most obvious deformation feature produced during the triaxial deformation of consolidated samples are grain boundary, opening-mode cracks (gbo cracks). An opening mode is easily identified if the grain boundary geometry on the two sides of the opening match exactly, suggesting they were previously in contact (**Figure 9d, e**). The gbo cracks distribute uniformly across samples and preferentially orient parallel or sub-parallel to differential load axis (**Figure 11a**). In many cases two gbo cracks link by connecting to a common pore. The density, aperture, and linking of the gbo cracks increase with increasing inelastic strain, and linked crack arrays comprised of several gbo cracks develop at large axial strain (Ding et al., 2017). Intragranular cracking is minor and often associated with fluid inclusions. Some of the fluid inclusions in grain interior, shown as dark pits in micrograph, show greater opening than generally observed in consolidated samples suggesting cracking caused by differential loading (**Figure 11a**). In the consolidated sample deformed to an axial strain of 7.31%, only 7.6% of all grains contain intragranular cracks, which is slightly higher than the background intragranular cracks density of 6.4% observed at zero axial strain. Of all the intragranular cracks, 81% are associated with fluid inclusions.

Under transmitted-light microscopy, high-density and irregular-shaped fluid inclusions are observed at closed grain boundaries of deformed samples (Figure 9**Figure 10c, d**). The fluid inclusions appear in all closed grain boundaries. The morphology of the fluid inclusions is similar to that of the consolidated samples prior to triaxial deformation (compare **Figure 10b** with **d**).

Triaxial deformation of the annealed samples produced wavy slip lines in the initially strain-free halite grains (**Figure 9f**). The slip lines are mostly concentrated at grain contacts and their density is much lower than that in consolidated samples. Newly recrystallized grains are not observed in the annealed samples after triaxial deformation. Grain shape analysis shows similar minor-to-major axial ratio for an undeformed sample (0.652±0.154, 166 grains) and a sample triaxially deformed to 4.87% axial strain (0.652±0.165, 104 grains). The similar grain axial ratios suggest that grain flattening during triaxial deformation of the annealed sample is insignificant.

Grain boundary opening cracks are present in the deformed annealed samples (**Figure 11b**). Two sets of gbo cracks are identified. One set of gbo cracks are oriented at low angle to load axis, and occur as either isolated cracks along a single boundary between two grains, or a series of cracks linked in the direction of the differential load. This set of cracks are formed during triaxial deformation, and are similar to the gbo cracks linked at pores in the deformed consolidated samples. The other set of gbo cracks in the deformed annealed samples are oriented at various angles but linked in the direction perpendicular to the differential load axis. The second set were produced during depressurization of the sample at the end of the triaxial deformation experiment. Intragranular cracking is also minor in triaxially deformed annealed samples. In the sample deformed to 4.87% axial strain, 7.7% of total grains contain intragranular cracks.

Viewed under transmitted-light optical microscopy, high-density and spherical or tubular-shaped fluid inclusions are apparent at the closed grain boundaries of the triaxially deformed annealed samples (**Figure 10g, h**). The fluid inclusions appear in all closed grain boundaries. Comparing with the undeformed annealed samples, grain boundary fluid inclusions in the triaxially deformed annealed samples are less equant with more tubular shapes (compare **Figure 10f** with **h**).

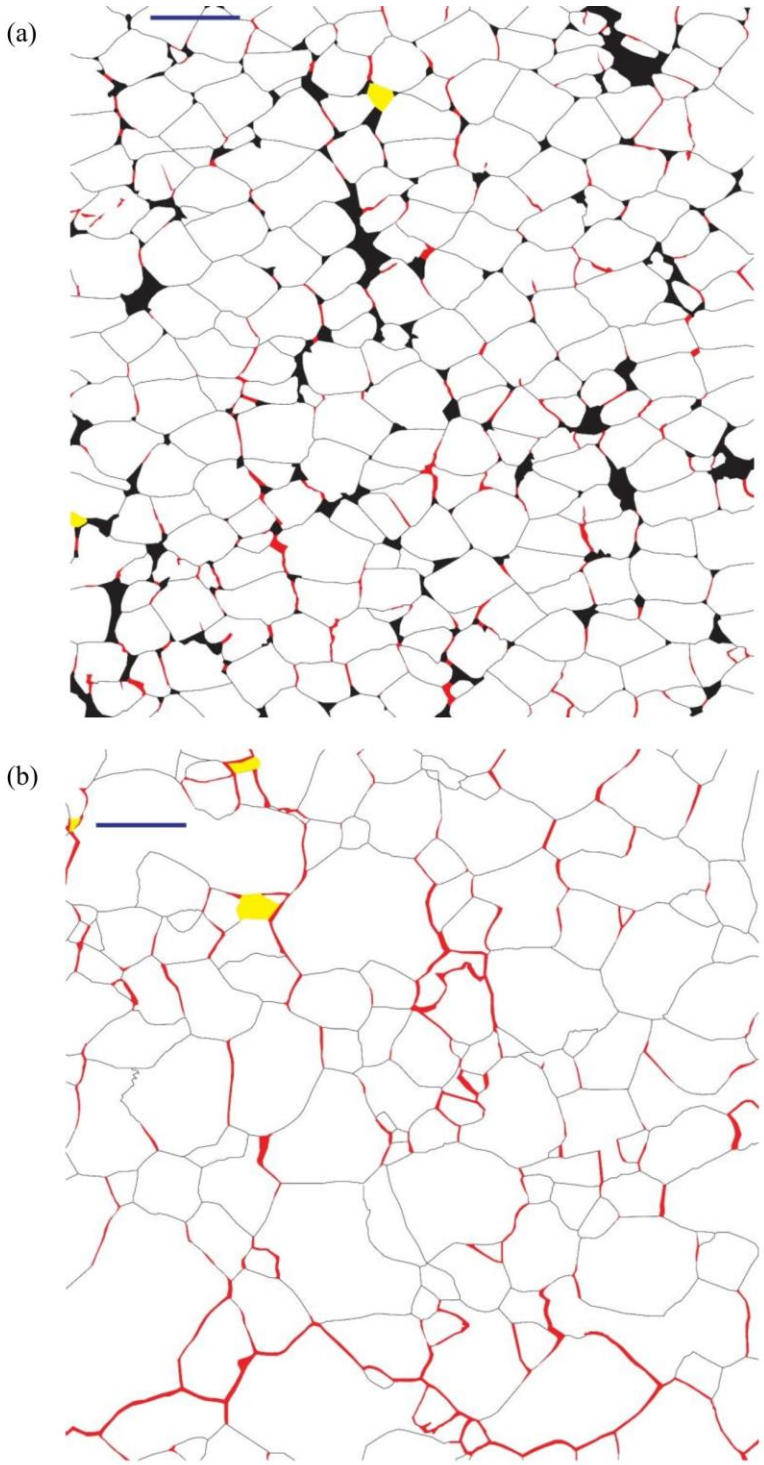

Figure 11. Stitched micrographs of (a) consolidated sample 61123 deformed to 7.31% axial strain and (b) annealed sample 70304 deformed to 4.87% axial strain. Halite grains (white), pores (black), and opening-mode microcracks (red) were manually traced. Missing grains (yellow) were caused by polishing. Scale bar (blue) represents 0.5 mm. Images were taken at sample center. Differential load axis was vertical. Note two sets of grain boundary openings in (b): one set preferentially aligned to load axis (vertical direction) and distributed across the micrograph; the other set connected in the direction perpendicular to load axis (horizontal direction) and localized at the bottom of the micrograph.

4 Discussion

4.1 Deformation mechanisms

In consolidated samples, intracrystalline plasticity is an active deformation mechanism during the cyclic triaxial compression tests. First, the density of wavy slip lines after triaxial deformation is increased beyond that seen in the grains deformed by consolidation only. Second, wavy slip lines are observed in the recrystallized grains formed at the end of consolidation, but are absent from the recrystallized grains formed at the end of triaxial deformation, also demonstrating dislocation motion during triaxial deformation. At room temperature, low confining pressure, and relatively fast strain rates, dislocation glide is the dominant intracrystalline plastic process in halite as recovery mechanisms are insufficient (Carter & Hansen, 1983; Peach & Spiers, 1996; Senseny et al., 1992). However, two lines of evidence indicate dislocation glide is a subordinate mechanism. During triaxial deformation, the stress-strain behavior showed nearly constant flow stress, but a characteristic behavior of deformation by dislocation glide is strain hardening. In addition, grain flattening is relatively insignificant in that it contributes only around 6% to the total axial strain.

Cracking, opening, and sliding along grain boundaries is significant during triaxial deformation of the consolidated samples. The gbo cracking occurs at all stages of axial shortening and is recorded by increase in crack density and aperture with increased axial strain (**Figure 11a**). Moreover, opening cracks produce the porosity that explains the observed dilatancy throughout triaxial deformation (**Figure 3a**). Based on the geometry and distribution of gbo cracks, shear motion can be documented in adjacent closed grain boundaries (**Figure 9e**). Here, we refer to the shear motion along grain boundaries with the descriptive term, grain boundary sliding (gbs), i.e. the mechanism of sliding is not implied. The creation and continued opening of the gbo cracks are accommodated by gbs at neighboring closed grain boundaries, forming linked arrays of gbo and gbs cracks. The combined operation of distributed gbo and gbs cracks can accommodate the triaxial deformation and lead to net porosity increase without the necessity of significant intragranular deformation and grain flattening. The observed micromechanisms of deformation indicate that grain boundaries are relatively weak planes when oriented at low to moderate angles to the differential load axis. During sample fabrication by uniaxial consolidation, the lateral stress is raised and dislocation density in the halite grains is dramatically increased and grains are hardened. Subsequent triaxial deformation at low confining pressure and room temperature promotes brittle processes along relatively weak grain boundaries. Thus, bonding at optimally oriented grain boundaries are progressively damaged and displaced with increasing inelastic deformation. Halite grains of broken boundaries rearrange through sliding and opening as a primary way to accommodate the triaxial deformation. That is, the linked operation of gbo and gbs is the dominant deformation mechanism during triaxial deformation of the consolidated samples.

Comparing to the microprocesses of deformation in the consolidated samples, intracrystalline plasticity is significantly more important for deformation of the annealed samples during the cyclic triaxial compression test. Static recovery and recrystallization during annealing reduce dislocation density resulting in strain-free grains and reduced critical shear stress for dislocation glide (**Figure 9f**). The triaxial deformation leads to dislocation motion evidenced by the formation of wavy slip lines (**Figure 9g**). While consolidated samples flow at nearly constant stress, annealed sample yields at much lower differential stress and show pronounced work

hardening in the stress-strain response (**Figure 3**), consistent with deformation by intracrystalline dislocation glide. In annealed samples, dislocation glide contributed more to the total deformation than in consolidated sample. Nonetheless, little evidence of grain flattening and a low density of slip lines in the sample deformed to 4.87% axial strain indicate that strain in the annealed samples is not homogeneous and dislocation glide is likely a subordinate deformation mechanism.

Cracking, opening, and sliding along grain boundaries also is important during the cyclic triaxial compression tests on annealed samples (**Figure 11b**), and increase in sample volume (**Figure 3b**) is also observed. While grain-scale plastic deformation by dislocation glide may have contributed gbo, there are also evidence that gbs facilitates the opening (**Figure 9g**) as occurred in the consolidated samples. Thus, optimally oriented grain boundaries are weak relative to the grain interiors of annealed samples at the test conditions. Minor intragranular cracking is observed in deformed annealed samples. Additionally, unloading-induced grain boundary cracking occurs in annealed sample as evinced by stress-strain response (**Figure 5c**) and microstructural observation (**Figure 11b**). The unloading process may also have affected the load-axis oriented grain boundary openings; but, considering the well-preserved preferential orientation, this effect is probably limited.

In annealed samples, strain partitioning between intracrystalline plastic and gbo and gbs processes changes with axial strain during the cyclic triaxial compression tests. With increasing inelastic strain, the slope of the stress-strain curve decreases while the slope of volumetric strain-axial strain curve increases (**Figure 3b**), which indicates that the hardening rate decreases while dilatancy rate increases. In the early stage of deformation, dislocation glide is easy in strain-free grains. With increasing dislocation density, continued glide requires higher stress which can enhance gbs and gbo. For the sample with a total axial strain of 4.87%, we infer that gbo and gbs is dominant relative to dislocation glide based on the microstructure observation of pronounced grain boundary cracks, insignificant grain flattening, and a low density of slip lines. Using similar synthetic salt-rock sample and test conditions, grain boundary cracking and intracrystalline plasticity also are documented by Peach and Spiers (1996) and Bourcier et al. (2013). While Peach and Spiers (1996) focused on the effect of microcracking in transport properties of salt-rock, (Bourcier et al., 2013) quantified strain partitioning between gbs and intracrystalline plasticity using surface markers and digital image correlation. These works conclude that gbs accounts for more than 50% of total strain in fine-grained (0.03-0.08 mm) samples, and intracrystalline plasticity accounts for more than 80% in coarse-grained (0.25-0.5 mm) samples. Given that our annealed samples have a greater range of grain size (0.025-0.833 mm), and were deformed to a greater total strain ~8% relative to ~3%, our interpretation of dominant deformation mechanism is in good agreement with previous findings.

Both consolidated and annealed samples deform in the semibrittle flow field with a combined and linked operation of intracrystalline-plastic mechanisms, gbo cracking, intragranular cracking, and gbs. While intragranular cracking is minor in both types of samples, the relative importance of the other mechanisms is possibly quite different. In consolidated samples, grain boundary cracking is the dominant deformation mechanism for all axial strains achieved. In annealed samples, strain partitioning between grain boundary cracking and dislocation glide is dependent on total inelastic strain; grain boundary cracking is enhanced with increasing strain relative to dislocation glide because of work-hardening associated with glide. In some ways, the consolidated sample may be viewed as representative of the final state of an

annealed sample deformed at rates and temperatures where recovery processes are relatively slow and unimportant. When dislocation density in annealed sample becomes high enough after sufficient inelastic deformation, dislocation glide would be largely inhibited while grain boundary cracking and sliding becomes dominant, which is a state of deformation processes in the consolidated samples during semibrittle flow.

4.2 Micromechanisms of grain boundary sliding

In the brittle field, slip along grain boundaries displays frictional behavior (pressure dependence of shear strength) arising from microfracture and local separation along non-planar surfaces such that the true area of contact is less than the apparent area (Bowden & Tabor, 2001; Scholz, 2019). Locally, associated with indentation creep at contacting asperities, intracrystalline processes such as dislocation glide also may occur (Dieterich, 1978). At room temperature, low confinement, and high strain rates, shear of granular salt displays frictional behavior with microstructural evidence of fracture, grain crushing, and intracrystalline plasticity, and macroscopic coefficient of friction between 0.5 and 1 (Chester & Logan, 1990; Shimamoto, 1986). These studies demonstrate an increase in the role of intracrystalline plasticity and concomitant reduction in friction coefficient with increased pressure and decreased strain rate (Chester, 1988; Shimamoto, 1986). Accordingly, in the present triaxial experiments at low confining pressure and observation of gbo cracking, it is likely that associated gbs is frictional.

For the consolidated samples, the accumulation of permanent strain during the large stress cycles occurs at a semibrittle flow (differential stress) of 40 MPa and confining pressure of 1 MPa. Given this stress state, and assuming stress homogeneity, the shear and normal stress on grain boundaries at angles to the sample axis of 45˚ or less would satisfy a sliding friction coefficient of greater than ~1. Grain boundaries deemed likely to have slipped in the deformed samples, based on linkage to pores or neighboring gbo cracks, have an average orientation of 50.4° and 53.4° to the sample axis in the consolidated and annealed samples, respectively. For these and greater angles, friction sliding on grain boundaries is compatible with the range of friction coefficients observed in shear experiments on granular salt. Thus, for semibrittle flow during the large stress cycles in both sample types, gbs is likely frictional and deformation is dominated by grain movement along the linked gbs and gbo crack networks throughout the sample. Given the irregularity and non-planarity of the linked crack networks, the local stresses are likely variable. As such, the lower semibrittle flow strength observed for the annealed samples may reflect accommodation of geometric strain incompatibilities via intracrystalline plasticity in the less-hardened grains.

Frictional sliding generally is characterized by small magnitude rate-dependence (Dieterich, 1978; Marone, 1998). Although the macroscopic semibrittle flow stress in stress cycling experiments was determined at only a single strain rate, stress-relaxation tests can provide information on rate dependence and the underlying mechanisms of sliding. Small magnitude rate dependence of friction is reflected by large stress exponents during relaxation. The behavior documented here is consistent with friction at the beginning of relaxation (i.e. at high stress) for both sample types. The marked change in slope for the consolidated sample to a very small stress exponent is indicative of a change in the underlying process of gbs; whereas the consistent slope in the annealed sample suggests frictional sliding at all rates tested (to 10^{-10} s^{-1}).

The consolidated samples are considered water wet, with a water content of 301 ppm (weight $H_2O/10^6$ NaCl). For fine-grained salt-rocks (0.08-2 mm), this water content is sufficient

to invoke fluid-assisted grain boundary processes such as grain boundary migration recrystallization and solution-transfer creep as long as the water is located at the grain boundaries (Shen & Arson, 2019a; Spiers & Carter, 1996; Ter Heege et al., 2005; Watanabe & Peach, 2002). We infer that at low strain rates, gbs may be accommodated by fluid-assisted diffusion if water is distributed along the sliding grain boundaries. The fluid-assisted diffusional process is likely highly local and serves as an effective accommodation mechanism for gbs (Bos & Spiers, 2002a; Pennock et al., 2006; Raj & Ashby, 1971), and is compatible with the stress relaxation behavior at low strain rates with a stress exponent of nearly one (**Figure 8**). Microstructure observations of the consolidated samples prior to triaxial deformation documents the presence of numerous fluid-inclusions along the grain boundaries, as well as in the interior of the grains. Activation of frictional sliding on grain boundaries during semibrittle flow releases and distributes the water from inclusions to form thin fluid films within which diffusive mass transfer can occur at the reduced strain rates achieved during stress relaxation tests.

The rate-dependence of gbs is clearly different for consolidated and annealed samples as shown by the stress relaxation tests (**Figure 8**). The water content of the annealed samples is 5.1 ppm (weight $H_2O/10^6$ NaCl) prior to triaxial deformation. Several ppm of water is comparable with the "dry samples" of Watanabe & Peach (2002), which deform without the operation of fluid-assisted grain boundary processes (Bos & Spiers, 2002a; Pennock et al., 2006). By comparison, gbs accommodated by fluid-assisted diffusion is likely negligible in the annealed sample, which is supported by the high stress exponent (i.e., 25.4) in the stress relaxation test at all strain rates (**Figure 8**). At high strain rates, at the onset of stress relaxation, the stress exponent of the consolidated samples is clearly lower than that of annealed samples. This suggests that the solution-transfer processes dominating gbs at low rates also are likely contributing to, though not dominating, frictional gbs in consolidated samples during semibrittle flow.

4.3 Grain boundary behavior and elasticity

The changes in the elastic properties in both types of samples from triaxial deformation, as displayed in the small-load cycles, must be caused by changes in pores, along grain boundaries, or within grain interiors. The observation that elastic properties are largely restored to that of the starting samples, after sufficiently long holds at confinement of 1 MPa or less, suggests changes in elastic behavior was controlled by grain boundary processes. Before and after holds, no appreciable microstructural change was observed in the grain interior such as the density and distribution of dislocation, or at intragranular cracks and pores. However, we infer there is an important change at grain boundaries during a hold, specifically healing and rebonding of grain boundaries that slipped frictionally during semibrittle flow.

In the triaxial deformed samples, grain boundaries can be classified into two groups based on whether they open under differential load (**Figure 12**). Grain boundaries that open and create new porosity are preferentially aligned to load axis. Grain boundaries that remain closed can be further divided into two subgroups based on whether sliding occurs. Those oriented at low to moderate angles to load axis are subjected to sufficient shear stress to cause sliding during differential loading, while those oriented at high angles are not. The changes in elastic properties are well correlated with the quality of bonding of the closed grain boundaries oriented appropriately for sliding and linked to boundaries oriented for opening.

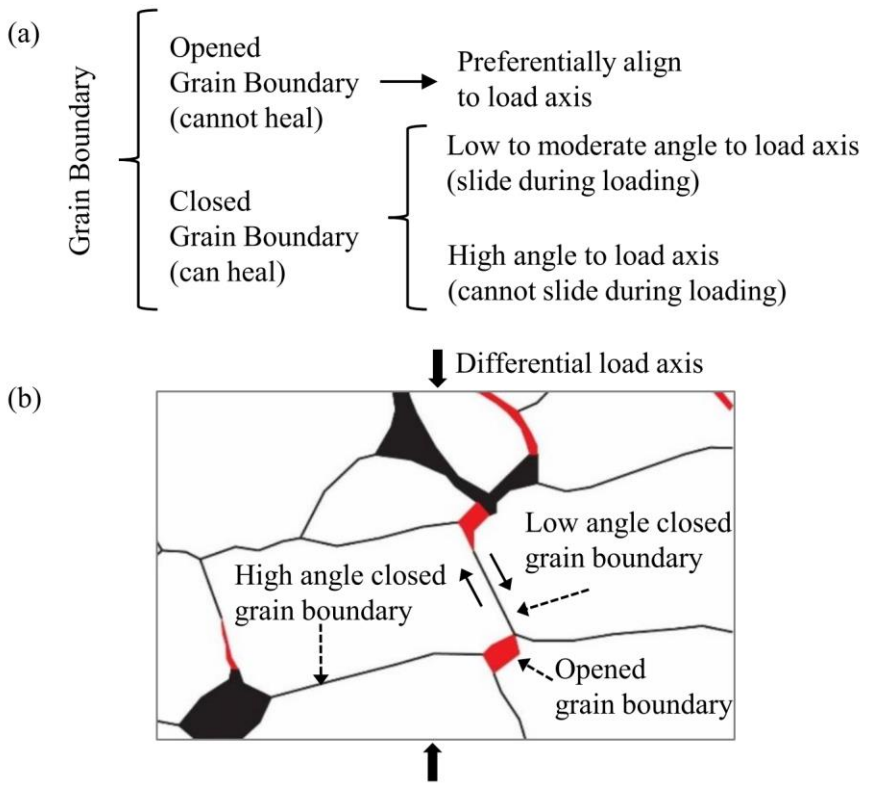

Figure 12. Classification of grain boundaries in deformed samples: (a) classification chart and (b) microstructural examples. In (b) halite grains (white), pores (black), and opening-mode microcracks (red) were manually traced. Paired arrows show inferred shear motion at a closed grain boundary.

For both types of samples, Young's modulus and Poisson's ratio measured during small-load cycles decreases and increases, respectively, with increasing inelastic deformation by semibrittle flow. Both elastic properties recover to nearly original values (i.e., at zero axial strain) after the sample is allowed to heal. Healing of closed grain boundaries in dry annealed samples is much slower, even under load, than in the wet consolidated samples, suggesting healing is a fluid-assisted process. Microstructural observation of healed boundaries that had slid (evinced by linkage to opened boundaries) shows dense arrays of small fluid inclusions characteristic of crack-healing (**Figure 10d, h**; Roedder, 1984). Opened grain boundaries remain open and do not show evidence of rebonding (**Figure 9d, e**). Healed boundaries are restrengthened, so they do not slip at low loads. With resumed differential loading to invoke semibrittle flow (large-load cycles), the appropriately oriented boundaries are rebroken and frictional sliding ensues. With continued semibrittle flow, more boundaries are activated leading to progressive changes in elastic properties (**Figure 6**). Collectively, these observations indicate that the changes in elastic properties are largely controlled by the microprocesses of sliding on the closed, inclined grain boundaries.

After finite strain by semibrittle flow in consolidated samples, elastic properties exhibit rate-dependence during small stress cycling. Cycling at lower strain rate leads to lowered modulus and greater hysteresis. The rate-dependence increases with increasing inelastic axial strain almost disappears upon healing (**Figure 6a, b**). These observations can be understood by the fluid-assisted diffusional processes in sliding grain boundaries. In the small-load cycles, more

pronounced diffusion at low strain rates leads to greater viscoelastic behavior. In a stress-strain plot, this is expressed as lower stiffness (more axial strain is recovered) and higher hysteresis (more work is done) (**Figure 4b, d**). Increasing semibrittle flow at large-load cycles activates more sliding grain boundaries, which in turn leads to more pronounced hysteresis, rate-dependence, and anelasticity in small-load cycles. These phenomena are absent in annealed samples due to insufficient water at grain boundaries.

4.4 Implications

Our experiments document significant transient behaviors associated with stress cycling, which can be explained by path-dependent activation of water-assisted diffusion processes and termination by static healing. Numerical modeling of our experimental data also demonstrates the association of transient semibrittle behavior with stress cycling (Shen et al., 2020). In nature, stress cycling is common in energy storage salt caverns and seismogenic zones where semibrittle deformation occurs. The periodic changes in deformation microprocesses could have profound implications for structural integrity of salt caverns and earthquake mechanics.

In salt caverns, similar conditions of low temperature and confining pressure may be encountered at cavern walls (Bérest, 2013; Brouard et al., 2012; Wang et al., 2018a). In excavated salt caverns, halite grains at walls increase in dislocation density due to construction related deformation, whereas in solution mined caverns dislocation density in halite grains at walls should be as low as in non-disturbed natural salt (Fokker, 1995). In gas storage caverns operated to satisfy the seasonal or emergency needs, the cyclic loading associated with changes in gas volume will induce stress cycling (Bérest, 2013) analogous to our experiments. Inelastic deformation from large stress cycles around salt cavern walls could lead to the development of grain boundary cracking and frictional sliding to redistribute water, which can activate viscous processes. Linking of preferentially opened grain boundaries with shear slipping boundaries can produce linked arrays that, with further stress cycling, could cause instability of cavern wall such as spalling and block fall (Ding et al., 2017). Avoidance of large stress cycling could minimize breakage and activation of frictional sliding with dilatancy from associated opening boundaries, and employing holds to allow stress relaxation and healing of cracked grain boundary could help preserve the integrity of cavern walls. Additionally, as water is almost always present in natural salt rocks (Roedder, 1984), elastic deformation may be dependent on loading rate with pronounced hysteresis at low strain rates in between stress cycles. Numerical modeling of salt caverns should consider the time-dependent behavior of salt and the consequent damage and healing processes, which will affect the mechanical behavior and sealing capability of salt caverns (Arson, 2020; Shen & Arson, 2019b).

In the lithosphere, the brittle-ductile transition is characterized by semibrittle deformation involving brittle frictional, crystal-plastic, and diffusional processes (Brace & Kohlstedt, 1980; Kirby, 1980; Kohlstedt et al., 1995). In seismogenic zones of the crust, the brittle-ductile transition corresponds to the depth limit of shallow crustal seismicity and experiences pronounced stress cycling (Brace & Kohlstedt, 1980; Sibson, 1983). In deep crust, there are also evidences of elevated pore pressure which is thought to enhance brittle deformation despite high stress and temperature conditions (Beeler et al., 2016). During inter-seismic periods, the upper part of brittle-ductile transition deforms dominantly by brittle friction and accumulate stress, whereas the lower part deforms viscously near steady state (Scholz, 2019; Sibson, 1983, 1986). Viewing salt as rock analogue material, the consolidated samples may represent the shallower

brittle frictional rock end member of the semibrittle regime, and the annealed samples may represent the deeper viscously creeping rock end member. Earthquakes rupture downward into the semibrittle zone, effectively creating large displacement and concentrated increase in stress and strain rates (Strehlau, 1986), which may be qualitatively analogous to the large-load cycles employed in this study. The pronounced stress cycling by earthquakes may cause the healed or recrystallized rocks to yield and undergo semibrittle flow, activating grain boundaries and redistributing water. Post-seismic deformation may involve time-dependent gbs that effectively relax increased stress. As stress is reduced, rocks may eventually heal at grain boundaries at shallow depths or transition back to steady state creep with recrystallization before next stress cycle. Consequently, profound transient perturbation in the lithosphere could activate completely different deformation microprocesses that alter rock rheological behavior during seismic cycles. Certainly, this is a rather simplified analogy to natural rock deformation by ignoring many factors such as rock composition and heterogeneity. However, it serves to illustrate the important role of grain boundary processes in controlling rheological behavior of rock at semibrittle conditions.

5 Conclusions

We conducted cyclic triaxial compression and stress relaxation tests on two types of synthetic salt-rocks with contrasting grain structures at room temperature and low confinement. Mechanical behavior and microstructures document semibrittle deformation in both samples involving grain boundary opening and sliding, dislocation glide, intragranular cracking. Large stress cycling activates grain boundary sliding accommodated by frictional processes at high strain rates and/or dry condition, or by pronounced fluid-assisted diffusion at low strain rates and presence of fluid. Young's modulus and Poisson's ratio are largely controlled by the microprocesses at closed grain boundaries, leading to viscoelastic and hysteretic behaviors. Such time-dependent effects vanish with grain boundary healing over days-long holds at low differential stress. The observed transient semibrittle processes in response to stress and strain rate cycling suggest that transient perturbation in the lithosphere could activate different deformation microprocesses that alter rock rheological behavior during seismic cycles, and that frequent large stress cycles in salt caverns could damage their structural integrity.

Acknowledgments

The authors are grateful to Chris Spiers, Colin Peach, Peter van Krieken and others at Utrecht University for guidance in salt microscopy techniques. Special thanks go to Andreas Kronenberg for assistance in measuring water content and numerous illuminating discussions. Financial support for this research was provided by the National Science Foundation, Awards CMMI-1361996 (TAMU) and CMMI-1362004 (GT). The data used in this study are available at the Texas Data Repository (https://doi.org/10.18738/T8/QCHJEM).

References

Arson, C. (2020). Micro-macro mechanics of damage and healing in rocks. *Open Geomechanics*, *2*, 1-41. https://doi.org/10.5802/ogeo.4.

Beeler, N. M., Hirth, G., Thomas, A., & Bürgmann, R. (2016). Effective stress, friction, and deep crustal faulting. *Journal of Geophysical Research: Solid Earth*, *121*, 1040-1059. https://doi.org/10.1002/2015JB012115.

Bérest, P. (2013). *The mechanical behavior of salt and salt caverns*. Paper presented at ISRM International Symposium - EUROCK 2013, International Society for Rock Mechanics and Rock Engineering, Wroclaw, Poland.

Bos, B., & Spiers, C. J. (2002a). Fluid-assisted healing processes in gouge-bearing faults: Insights from experiments on a rock analogue system. *Pure and Applied Geophysics*, *159*, 2537-2566. https://doi.org/10.1007/s00024-002-8747-2.

Bos, B., & Spiers, C. J. (2002b). Frictional-viscous flow of phyllosilicate-bearing fault rock: Microphysical model and implications for crustal strength profiles. *Journal of Geophysical Research: Solid Earth*, *107*(B2), ECV 1-1-ECV 1-13. https://doi.org/10.1029/2001JB000301.

Bourcier, M., Bornert, M., Dimanov, A., Héripré, E., & Raphanel, J. L. (2013). Multiscale experimental investigation of crystal plasticity and grain boundary sliding in synthetic halite using digital image correlation. *Journal of Geophysical Research: Solid Earth*, *118*, 511-526. https://doi.org/10.1002/jgrb.50065.

Bowden, F. P., & Tabor, D. (2001). *The friction and lubrication of solids.* Oxford, England: Oxford University Press.

Brace, W. F., & Kohlstedt, D. L. (1980). Limits on lithospheric stress imposed by laboratory experiments. *Journal of Geophysical Research: Solid Earth*, *85*, 6248-6252. https://doi.org/10.1029/JB085iB11p06248.

Brouard, B., Bérest, P., Djizanne, H., & Frangi, A. (2012). Mechanical stability of a salt cavern submitted to high-frequency cycles. In P. Bérest, M. Ghoreychi, F. Hadj-Hassen and M. Tijani (Eds.), *The Mechanical Behavior of Salt VII*. Paris, France: Taylor & Francis Group.

Carter, N. L., & Hansen, F. D. (1983). Creep of rocksalt. *Tectonophysics*, *92*, 275-333. https://doi.org/10.1016/0040-1951(83)90200-7.

Carter, N. L., & Kirby, S. H. (1978). Transient creep and semibrittle behavior of crystalline rocks. *Pure and Applied Geophysics*, *116*, 807-839. https://doi.org/10.1007/BF00876540.

Chester, F. M. (1988). The brittle-ductile transition in a deformation-mechanism map for halite. *Tectonophysics*, *154*(1), 125-136. https://doi.org/10.1016/0040-1951(88)90230-2.

Chester, F. M. (1989). Dynamic recrystallization in semi-brittle faults. *Journal of Structural Geology*, *11*(7), 847-858. https://doi.org/10.1016/0191-8141(89)90102-8.

Chester, F. M., & Logan, J. (1990). Frictional faulting in polycrystalline halite: Correlation of microstructure, mechanisms of slip, and constitutive behaviour, in A. G. Duba, W. B. Durham, J. W. Handin and H. F. Wang (Eds.), *The Brittle-Ductile Transition in Rocks: The Heard Volume*, *Geophysical Monograph Series* (Vol. 56, pp. 49-65). Washington, DC: American Geophysical Union.

Coble, C., French, M., Chester, F., Chester, J., & Kitajima, H. (2014). In situ frictional properties of San Andreas Fault gouge at SAFOD. *Geophysical Journal International*, *199*(2), 956-967. https://doi.org/10.1093/gji/ggu306.

Desbois, G., Urai, J. L., Burkhardt, C., Drury, M. R., Hayles, M., & Humbel, B. (2008). Cryogenic vitrification and 3D serial sectioning using high resolution cryo-FIB SEM technology for brine-filled grain boundaries in halite: First results. *Geofluids*, *8*, 60-72. https://doi.org/10.1111/j.1468-8123.2007.00205.x.

Dieterich, J. H. (1978). Time-dependent friction and the mechanics of stick-slip. *Pure and Applied Geophysics*, *116*(4), 790-806. https://doi.org/10.1007/BF00876539.

Ding, J. (2019). Grain Boundary and Elastic Behavior in Semi-brittle Synthetic Salt-rock, (Doctoral dissertation). Retrieved from OAKTrust. (http://hdl.handle.net/1969.1/184425). College Station, TX: Texas A&M University.

Ding, J., Chester, F. M., & Chester, J. S. (2017). *Microcrack network development in salt-rock during cyclic loading at low confining pressure*. Paper presented at 51st U.S. Rock Mechanics/Geomechanics Symposium, American Rock Mechanics Association, San Francisco, CA.

Ding, J., Chester, F. M., Chester, J. S., Zhu, C., & Arson, C. (2016). *Mechanical behavior and microstructure development in consolidation of nominally dry granular salt*. Paper presented at 50th U.S. Rock Mechanics/Geomechanics Symposium, American Rock Mechanics Association, Houston, TX.

Ellis, S., & Stöckhert, B. (2004). Elevated stresses and creep rates beneath the brittle-ductile transition caused by seismic faulting in the upper crust. *Journal of Geophysical Research: Solid Earth*, *109*(B5). https://doi.org/10.1029/2003jb002744.

Fokker, P. A. (1995). The behaviour of salt and salt caverns, (Doctoral dissertation). Retrieved from TUDelft Institutional Repository. (http://resolver.tudelft.nl/uuid:6847f8e4-3b09-4787-be02-bcce9f0eed06). Delft, Netherlands: Delft University of Technology.

Fredrich, J. T., Evans, B., & Wong, T. F. (1989). Micromechanics of the brittle to plastic transition in Carrara marble. *Journal of Geophysical Research: Solid Earth*, *94*, 4129-4145. https://doi.org/10.1029/JB094iB04p04129.

French, M. E., Chester, F. M., & Chester, J. S. (2015). Micromechanisms of creep in clay-rich gouge from the Central Deforming Zone of the San Andreas Fault. *Journal of Geophysical Research: Solid Earth*, *120*, 827-849. https://doi.org/10.1002/2014JB011496.

Fusseis, F., & Handy, M. R. (2008). Micromechanisms of shear zone propagation at the brittle–viscous transition. *Journal of Structural Geology*, *30*(10), 1242-1253. https://doi.org/10.1016/j.jsg.2008.06.005.

Ghahremani, F. (1980). Effect of grain boundary sliding on anelasticity of polycrystals. *International Journal of Solids and Structures*, *16*, 825-845. https://doi.org/10.1016/0020-7683(80)90052-9.

Hadizadeh, J., & Tullis, J. (1992). Cataclastic flow and semi-brittle deformation of anorthosite. *Journal of Structural Geology*, *14*, 57-63. https://doi.org/10.1016/0191-8141(92)90144-L.

Haupt, M. (1991). A constitutive law for rock salt based on creep and relaxation tests. *Rock Mechanics and Rock Engineering*, *24*(4), 179-206. https://doi.org/10.1007/BF01045031.

Hirth, G., & Tullis, J. (1994). The brittle-plastic transition in experimentally deformed quartz aggregates. *Journal of Geophysical Research: Solid Earth*, *99*, 11731-11747. https://doi.org/10.1029/93JB02873.

Hunsche, U., & Hampel, A. (1999). Rock salt — the mechanical properties of the host rock material for a radioactive waste repository. *Engineering Geology*, *52*(3), 271-291. https://doi.org/10.1016/S0013-7952(99)00011-3.

Ivins, E. R. (1996). Transient creep of a composite lower crust: 2. A polymineralic basis for rapidly evolving postseismic deformation modes. *Journal of Geophysical Research: Solid Earth*, *101*(B12), 28005-28028. https://doi.org/10.1029/96jb02846.

Kirby, S. H. (1980). Tectonic stresses in the lithosphere: Constraints provided by the experimental deformation of rocks. *Journal of Geophysical Research: Solid Earth*, *85*, 6353-6363. https://doi.org/10.1029/JB085iB11p06353.

Kirby, S. H., & Kronenberg, A. K. (1984). Deformation of clinopyroxenite: Evidence for a transition in flow mechanisms and semibrittle behavior. *Journal of Geophysical Research: Solid Earth*, *89*, 3177-3192. https://doi.org/10.1029/JB089iB05p03177.

Kitajima, H., Chester, F. M., & Biscontin, G. (2012). Mechanical and hydraulic properties of Nankai accretionary prism sediments: Effect of stress path. *Geochemistry, Geophysics, Geosystems*, *13*(10). https://doi.org/10.1029/2012GC004124.

Knipe, R. J. (1989). Deformation mechanisms - recognition from natural tectonites. *Journal of Structural Geology*, *11*, 127-146. https://doi.org/10.1016/0191-8141(89)90039-4.

Kohlstedt, D. L., Evans, B., & Mackwell, S. J. (1995). Strength of the lithosphere: Constraints imposed by laboratory experiments. *Journal of Geophysical Research: Solid Earth*, *100*, 17587-17602. https://doi.org/10.1029/95JB01460.

Lux, K., & Dresen, R. (2012). Design of salt caverns for high frequency cycling of storage gas. In P. Bérest, M. Ghoreychi, F. Hadj-Hassen and M. Tijani (Eds.), *The Mechanical Behavior of Salt VII*. Paris, France: Taylor & Francis Group.

Marone, C. (1998). Laboratory-derived friction laws and their application to seismic faulting. *Annual Review of Earth and Planetary Sciences*, *26*(1), 643-696. https://doi.org/10.1146/annurev.earth.26.1.643.

Marti, S., Stünitz, H., Heilbronner, R., Plümper, O., & Drury, M. (2017). Experimental investigation of the brittle-viscous transition in mafic rocks – Interplay between fracturing, reaction, and viscous deformation. *Journal of Structural Geology*, *105*, 62-79. https://doi.org/10.1016/j.jsg.2017.10.011.

Matysiak, A. K., & Trepmann, C. A. (2012). Crystal–plastic deformation and recrystallization of peridotite controlled by the seismic cycle. *Tectonophysics*, *530-531*, 111-127. https://doi.org/10.1016/j.tecto.2011.11.029.

Minkley, W., Knauth, M., Fabig, T., & Farag, N. (2015). Stability and integrity of salt caverns under consideration of hydro-mechanical loading. In L. Roberts, K. Mellegard and F. Hansen (Eds.), *The Mechanical Behavior of Salt VIII*. Paris, France: Taylor & Francis Group.

Mitra, G. (1984). Brittle to ductile transition due to large strains along the White Rock thrust, Wind River mountains, Wyoming. *Journal of Structural Geology*, *6*(1), 51-61. https://doi.org/10.1016/0191-8141(84)90083-X.

Munson, D. E., Chan, K. S., & Fossum, A. F. (1999). *Fracture and healing of rock salt related to salt caverns*. Paper presented at SMRI Spring Meeting, Solution Mining Research Institute, Las Vegas, NV.

Niemeijer, A., Marone, C., & Elsworth, D. (2008). Healing of simulated fault gouges aided by pressure solution: Results from rock analogue experiments. *Journal of Geophysical Research: Solid Earth*, *113*(B4). https://doi.org/10.1029/2007JB005376.

Noda, H., & Takahashi, M. (2016). The effective stress law at a brittle-plastic transition with a halite gouge layer. *Geophysical Research Letters*, *43*(5), 1966-1972. https://doi.org/10.1002/2015GL067544.

Nüchter, J., & Stöckhert, B. (2008). Coupled stress and pore fluid pressure changes in the middle crust: Vein record of coseismic loading and postseismic stress relaxation. *Tectonics*, *27*(1). https://doi.org/10.1029/2007TC002180.

Ozarslan, A. (2012). Large-scale hydrogen energy storage in salt caverns. *International Journal of Hydrogen Energy*, *37*(19), 14265-14277. https://doi.org/10.1016/j.ijhydene.2012.07.111.

Paterson, M. S., & Wong, T.-f. (2005). *Experimental rock deformation-the brittle field. 2nd ed.* Berlin, Germany: Springer-Verlag Berlin Heidelberg.

Peach, C. J., & Spiers, C. J. (1996). Influence of crystal plastic deformation on dilatancy and permeability development in synthetic salt rock. *Tectonophysics*, *256*, 101-128. https://doi.org/10.1016/0040-1951(95)00170-0.

Pec, M., Stünitz, H., Heilbronner, R., & Drury, M. (2016). Semi-brittle flow of granitoid fault rocks in experiments. *Journal of Geophysical Research: Solid Earth*, *121*, 1677-1705. https://doi.org/10.1002/2015JB012513.

Pennock, G. M., Drury, M. R., Peach, C. J., & Spiers, C. J. (2006). The influence of water on deformation microstructures and textures in synthetic NaCl measured using EBSD. *Journal of Structural Geology*, *28*, 588-601. https://doi.org/10.1016/j.jsg.2006.01.014.

Raj, R., & Ashby, M. F. (1971). On grain boundary sliding and diffusional creep. *Metallurgical Transactions*, *2*, 1113-1127. https://doi.org/10.1007/BF02664244.

Reber, J. E., Lavier, L. L., & Hayman, N. W. (2015). Experimental demonstration of a semi-brittle origin for crustal strain transients. *Nature Geoscience*, *8*, 712. https://doi.org/10.1038/ngeo2496.

Reber, J. E., & Pec, M. (2018). Comparison of brittle- and viscous creep in quartzites: Implications for semi-brittle flow of rocks. *Journal of Structural Geology*, *113*, 90-99. https://doi.org/10.1016/j.jsg.2018.05.022.

Roedder, E. (1984). The fluids in salt. *American Mineralogist*, *69*, 413-439.

Rutter, E. H., Atkinson, B. K., & Mainprice, D. H. (1978). On the use of the stress relaxation testing method in studies of the mechanical behaviour of geological materials. *Geophysical Journal of the Royal Astronomical Society*, *55*, 155-170. https://doi.org/10.1111/j.1365-246X.1978.tb04754.x.

Salzer, K., Popp, T., & Böhnel, H. (2007). Mechanical and permeability properties of highly pre-compacted granular salt bricks. In M. Wallner, K.-H. Lux, W. Minkley and H. R. J. Hardy (Eds.), *The Mechanical Behavior of Salt – Understanding of THMC Processes in Salt*. Paris, France: Taylor & Francis Group.

Scholz, C. H. (2019). *The mechanics of earthquakes and faulting.* Cambridge, United Kingdom: Cambridge University Press.

Senseny, P. E., Hansen, F. D., Russell, J. E., Carter, N. L., & Handin, J. W. (1992). Mechanical-Behavior of Rock Salt - Phenomenology and Micromechanisms. *International Journal of Rock Mechanics and Mining Sciences*, *29*, 363-378. https://doi.org/10.1016/0148-9062(92)90513-Y.

Shen, X., & Arson, C. (2019a). An isotropic self-consistent homogenization scheme for chemo-mechanical healing driven by pressure solution in halite. *International Journal of Solids and Structures*, *161*, 96-110. https://doi.org/10.1016/j.ijsolstr.2018.11.010.

Shen, X., & Arson, C. (2019b). Simulation of salt-cavity healing based on a micro–macro model of pressure solution. *Petroleum Geoscience*, *25*(3), 251-257. https://doi.org/10.1144/petgeo2018-094.

Shen, X., Arson, C., Ding, J., Chester, F. M., & Chester, J. S. (2020). Mechanisms of Anisotropy in Salt Rock Upon Microcrack Propagation. *Rock Mechanics and Rock Engineering*, 1-21. https://doi.org/10.1007/s00603-020-02096-1.

Shimamoto, T. (1986). Transition between frictional slip and ductile flow for halite shear zones at room temperature. *Science*, *231*(4739), 711-714. https://doi.org/10.1126/science.231.4739.711.

Shimamoto, T., & Noda, H. (2014). A friction to flow constitutive law and its application to a 2-D modeling of earthquakes. *Journal of Geophysical Research: Solid Earth*, *119*(11), 8089-8106. https://doi.org/10.1002/2014JB011170.

Sibson, R. H. (1977). Fault rocks and fault mechanisms. *Journal of the Geological Society*, *133*, 191-213. https://doi.org/10.1144/gsjgs.133.3.0191.

Sibson, R. H. (1983). Continental fault structure and the shallow earthquake source. *Journal of the Geological Society*, *140*, 741-767. https://doi.org/10.1144/gsjgs.140.5.0741.

Sibson, R. H. (1986). Earthquakes and rock deformation in crustal fault zones. *Annual Review of Earth and Planetary Sciences*, *14*, 149-175. https://doi.org/10.1146/annurev.ea.14.050186.001053.

Spiers, C. J., & Carter, N. L. (1996). Micorophysics of Rocksalt flow in nature. In M. Aubertin and J. H. R. Hardy (Eds.), *The Mechanical Behavior of Salt IV*. Clausthal-Zellerfeld, Germany: Trans Tech Publications.

Spiers, C. J., Schutjens, P. M. T. M., Brzesowsky, R. H., Peach, C. J., Liezenberg, J. L., & Zwart, H. J. (1990). Experimental determination of constitutive parameters governing creep of rocksalt by pressure solution. *Geological Society, London, Special Publications*, *54*, 215-227. https://doi.org/10.1144/GSL.SP.1990.054.01.21.

Spiers, C. J., Urai, J. L., Lister, G. S., Boland, J. N., & Zwart, H. J. (1986). *The influence of fluid-rock interaction on the rheology of salt rock*. Luxembourg: Commission of the European Communities.

Stewart, M., Holdsworth, R. E., & Strachan, R. A. (2000). Deformation processes and weakening mechanisms within the frictional–viscous transition zone of major crustal-scale faults: insights from the Great Glen Fault Zone, Scotland. *Journal of Structural Geology*, *22*(5), 543-560. https://doi.org/10.1016/S0191-8141(99)00164-9.

Strehlau, J. (1986). A discussion of the depth extent of rupture in large continental earthquakes. *Earthquake Source Mechanics, Geophysical Monograph Series*, *37*, 131-146. https://doi.org/10.1029/GM037p0131.

Ter Heege, J. H., De Bresser, J. H. P., & Spiers, C. J. (2005). Rheological behaviour of synthetic rocksalt: The interplay between water, dynamic recrystallization and deformation mechanisms. *Journal of Structural Geology*, *27*, 948-963. https://doi.org/10.1016/j.jsg.2005.04.008.

Tullis, J. A. (1979). High temperature deformation of rocks and minerals. *Reviews of Geophysics*, *17*, 1137-1154. https://doi.org/10.1029/RG017i006p01137.

Urai, J. L., Spiers, C. J., Zwart, H. J., & Lister, G. S. (1986). Weakening of rock salt by water during long-term creep. *Nature*, *324*, 554-557. https://doi.org/10.1038/324554a0.

Wang, T., Ma, H. L., Shi, X. L., Yang, C. H., Zhang, N., Li, J. L., et al. (2018a). Salt cavern gas storage in an ultra-deep formation in Hubei, China. *International Journal of Rock Mechanics and Mining Sciences*, *102*, 57-70. https://doi.org/10.1016/j.ijrmms.2017.12.001.

Wang, T., Yang, C., Chen, J., & Daemen, J. J. K. (2018b). Geomechanical investigation of roof failure of China's first gas storage salt cavern. *Engineering Geology*, *243*, 59-69. https://doi.org/10.1016/j.enggeo.2018.06.013.

Watanabe, T., & Peach, C. J. (2002). Electrical impedance measurement of plastically deforming halite rocks at 125°C and 50 MPa. *Journal of Geophysical Research: Solid Earth*, *107*, ECV 2-1-ECV 2-12. https://doi.org/10.1029/2001JB000204.

White, J. C., & White, S. H. (1983). Semi-brittle deformation within the Alpine fault zone, New Zealand. *Journal of Structural Geology*, *5*(6), 579-589. https://doi.org/10.1016/0191-8141(83)90070-6.

Zener, C. (1941). Theory of the elasticity of polycrystals with viscous grain boundaries. *Physical Review*, *60*, 906. https://doi.org/10.1103/PhysRev.60.906.

Zhang, X., Grupa, J., Spiers, C. J., & Peach, C. J. (2007). Stress relaxation experiments on compacted granular salt. In M. Wallner, K.-H. Lux, W. Minkley and H. R. J. Hardy (Eds.), *The Mechanical Behavior of Salt VI – Understanding of THMC Processes in Salt*. Paris, France: Taylor & Francis Group.

Zulauf, G. (2001). Structural style, deformation mechanisms and paleodifferential stress along an exposed crustal section: constraints on the rheology of quartzofeldspathic rocks at supra- and infrastructural levels (Bohemian Massif). *Tectonophysics*, *332*(1), 211-237. https://doi.org/10.1016/S0040-1951(00)00258-4.